Amundsen Sea Embayment accumulation variability measured with GNSS-IR

Andrew O. Hoffman[1], Michelle L. Maclennan[2], Jan Lenaerts[2], Kristine M. Larson[3,4], and
Knut Christianson[5]

[1]Lamont-Doherty Earth Observatory, Columbia University, Palisades, NY, USA
[2]National Center for Atmospheric Research, Boulder, CO, USA
[3]Institute of Geodesy and Geoinformation, University of Bonn, Bonn, Germany
[4]Aerospace Engineering Sciences, University of Colorado, Boulder, CO, USA
[5]Department of Earth and Space Sciences, University of Washington, Seattle, WA, USA

Correspondence: Andrew Hoffman (aoh2111@columbia.edu)

Abstract. ~~In order to~~ To improve projections of the future ice-sheet surface mass balance and the interpretation of the isotopic signals of past accumulation preserved in ice cores, it is critical to understand the mechanisms that transport water vapor to the Antarctic continent and lead to snowfall events. Global Navigation Satellite System (GNSS) receivers distributed across Antarctica to monitor ice velocity and solid Earth motion can be used to understand accumulation, ablation, and snow re-
5   distribution at the ice-sheet surface on sub-daily timescales. Here, we present a forward model for reflector height change between the GNSS antenna phase center and the snow surface and an inverse framework to determine accumulation rate and near-surface firn densification from the reflector height time series. We use this model to determine accumulation at ~~the sites of~~ three long-term ~~on-ice GNSS receivers~~ GNSS sites located in the Amundsen Sea Embayment (ASE) and at ~~a network~~ an array of GNSS receivers deployed in the 2007-2008 ~~, and~~ 2008-2009 ~~, and 2009-2010~~ austral summers. From the GNSS-IR accumu-
10   lation ~~reconstructions~~time series, we find that extreme precipitation (i.e. the 90th percentile of accumulation events) dominates total precipitation and that extreme event frequency varies seasonally. We use our GNSS-IR accumulation ~~reconstructions~~ time series together with reanalysis products to characterize the atmospheric conditions that promote extreme snowfall in the ASE. The blocking pressure systems that promote extreme accumulation on Thwaites Glacier are facilitated by tropical teleconnections, specifically convection that promotes Rossby waves trains from the Western Pacific, Indian, and Atlantic Oceans to the
15   Amundsen and Bellingshausen Seas.

1 Introduction

The mass balance of ice sheets and glaciers is defined as the difference between ice discharge~~and~~, surface mass balance (the sum of surface melt, sublimation, and snow accumulation), and grounded ice basal melt or accretion. Currently, the Antarctic ice sheet is losing mass at an accelerating pace due to changes ~~in ice discharge~~ primarily in West ~~Antarctica~~ Antarctic ice
20   discharge driven by oceanic warming and submarine ice-shelf melt (Velicogna et al., 2020; Smith et al., 2020). These changes in ice discharge have partially been offset by an increase in surface mass balance over much of the Antarctic Ice ~~sheet~~ Sheet since

the early 19th century (Kaspari et al., 2004; Frezzotti et al., 2013; Medley and Thomas, 2019). This due to a net increase in vapor moisture transport to the poles (Kaspari et al., 2004; Frezzotti et al., 2013; Thomas et al., 2015; Medley and Thomas, 2019). The positive trend in the difference between surface accumulation and surface mass loss from evaporation, sublimation, and

25 surface runoff surface mass balance is estimated to have led to the mitigation of mitigated sea-level rise by up to ~10 mm of sea-level rise in the 20th century (Medley and Thomas, 2019). In West Antarctica, where ice loss due to submarine melt has increased the most in recent decades, snow accumulation has

   Positive trends in surface accumulation may be particularly important in the Amundsen Sea Embayment (ASE), where enhanced accumulation may have the potential to impact and mitigate ice-sheet committed retreat (Davison et al., 2023).

30 Reduced models using constant surface mass balance and submarine melt rate forcing have suggested that the retrograde slope of the bed topography beneath the ice sheet in this region may promote unstable retreat (Weertman, 1974; Schoof, 2012). More recently, Sergienko and Haseloff (2023) showed that the spatial gradients of accumulation, especially gradients near the grounding zone, and accumulation variability (in addition to submarine melt variability) impact marine outlet glacier response and the variability of grounding-line retreat. Accumulation gradients near the grounding zones of vulnerable outlet glaciers and

35 drivers of these gradients are thus important to measure and accurately represent in climate simulations used to characterize the response of Antarctic outlet glaciers to climate change.

   Reanalysis remains the primary means of quantifying snowfall in Antarctica and has guided most of the atmospheric research and surface mass balance studies of West Antarctica in recent decades. Reanalysis techniques use archived observations with forecast models and data assimilation techniques to create gridded global datasets that describe the recent history of the

40 atmosphere, land surface, and ocean dynamics (i.e., Hersbach et al., 2020; Gelaro et al., 2017). The gridded nature of these products requires that they make coarse spatial assumptions for parameters such as vapor transport and snowfall that can vary spatially at scales that are relevant for glacier mass balance that are not well captured by reanalysis. Additionally, snow usually does not land where it falls in Antarctica (Lenaerts and van den Broeke, 2012). Reanalysis products typically assume that accumulation occurs in the location of precipitation. Even at the planetary scale, reanalysis products are not conservative.

45 The data assimilative techniques that are used to "nudge" solutions towards observations can introduce significant drift in moisture and energy budgets. Different reanalysis products also exhibit temperature and precipitation biases near the poles that vary between models. There are no long-term weather stations on Thwaites and Kohler Glaciers that record data assimilated into reanalyses, and there are very few studies that evaluate the performance of atmospheric reanalyses in comparison to observations. Ground-based observations of near-surface accumulation facilitate comparisons between reanalysis products that

50 can help distinguish physical processes from artifacts of these models and motivates model comparison with observations that are not assimilated directly into the reanalysis products.

   Accumulation of snowfall, the primary positive contributor to surface mass balance in West Antarctica, has typically been measured using records of accumulation preserved in englacial stratigraphy in ice-penetrating radar data, ice-core layering, and surface elevation change recorded by sonic snow surface loggers and expressed in satellite altimetry (i.e., Kaspari et al., 2004; Medley et al.

55 . Regional changes in the observed past accumulation suggest that the processes driving the snow accumulation increase across the Antarctic ice sheet are more complicated than the simple temperature-snow accumulation relationships that follow

from the capacity of a warmer atmosphere to hold more moisture (Fudge et al., 2016; Frieler et al., 2015). In addition to thermodynamic processes, snow accumulation variability has been connected to longer-term changes in atmospheric dynamics and circulation, and shorter-duration synoptic-scale dynamics that promote atmospheric river landfall and extreme precipitation

60 events (Dalaiden et al., 2020). Synoptic-scale mitigate ASE glacier mass loss due to ocean melt (Davison et al., 2023). Observations from shallow ice cores (i.e. Steig et al., 2005) and climate reanalysis (i.e. Davison et al., 2023) suggest that accumulation has increased in the Amundsen Sea Embayment over the last century, and that accumulation is strongly linked to spatial patterns of geopotential height in the Amundsen and Bellingshausen Sea sectors (Thomas et al., 2015). Regional variations in geopotential height have been linked to interactions between strong westerly circumpolar flow and ASE topography (Baines and Fraedrich, 1989; Walsh

65 , and global tropical teleconnections (Connolley, 1997; Renwick, 2002; Lachlan-Cope and Connolley, 2006; Ding et al., 2012; Turner et al . These interactions combine to form a persistent low pressure system known as the Amundsen Sea Low (ASL; Raphael, 2004; Turner et al. . The ASL is one of three low pressure systems distributed along the circumpolar trough (Connolley, 1997; Lachlan-Cope et al., 2001; Raph and exhibits a seasonal cycle in location and depth moving between the Amundsen and Bellingshausen Sea sectors between austral summer and austral winter (Fogt et al., 2012; Hosking et al., 2013; Turner et al., 2013). Changes in the position of this

70 low pressure system drive seasonal changes in moisture transport to West Antarctica in particular represents the dominant driver of snow accumulation derived from atmospheric reanalysis in West Antarctica and accounts for almost 50% of the accumulation variability (Dalaiden et al., 2020).

Observations of discrete snow accumulation events the Antarctic interior in climate reanalysis (Hosking et al., 2013; Maclennan and Lena . On average, precipitation in West Antarctica are important in order to further understand the synoptic drivers that cause

75 extreme precipitation in this region, especially on Thwaites Glacier, where extreme events determined from reanalysis contribute over half of the total accumulation (Maclennan and Lenaerts, 2021). Extensive efforts have been made to obtain a number of continuous atmospheric observations of Antarctica since the International Geophysical Year (IGY) in 1957-1958, when 50 predominately coastal weather stations were first deployed across the continent. Following the launch of the first Collected Localisation Satellite in 1978 and the establishment of the Argos program that marked the start of data telemetry, several

80 initiatives and programs began to erect permanent automatic weather stations (AWS) across Antarctica. Today, there are 267 AWS maintained across the continent. This still leaves much of the continent, and especially West Antarctica, sparsely sampled. Precipitation, a key variable for understanding surface mass balance, remains a notoriously difficult measurement to make and is still not routinely recorded across the AWS network. As a result, observations of accumulation in West Antarctica and Thwaites Glacier to date have also relied on records encoded in snow and firn, as preserved in firn and ice cores and englacial

85 stratigraphy imaged by ice-penetrating radar. increases in the austral winter when the ASL depth is greatest and the center of the low shifts southeastward closer to the ASE. Precipitation decreases in the summer when the low is weakest and shifts northwestward to the Amundsen-Ross sector (Fogt et al., 2012; Hosking et al., 2013; Turner et al., 2013).

1.1 Past Accumulation Studies in the ASE

The upper basin of the Thwaites Glacier was first visited for firn coring and near-surface radar data collection in the 2000-2001

90 austral summer as part of the International Trans-Antarctic Scientific Expedition (US-ITASE, Kaspari et al., 2004; Spikes et al., 2004)

. This ground-based traverse collected ice-penetrating radar profiles and a series of shallow firn/ice cores across the upper reaches of Thwaites and Pine Island Glaciers. Dated accumulation chronologies developed from the shallow core records and extended using englacial radiostratigraphy indicated that there had been an increase in accumulation ($\sim 5 - 10\%$) since 1970 in the western sector of the Pine Island –Thwaites drainage system and a slight decrease ($1 - 9\%$) in accumulation in sites near Marie Byrd Land and farther west (Kaspari et al., 2004; Spikes et al., 2004). The post-1970 increase in accumulation was strongly correlated with sea-level pressure, and was linked to the intensification of cyclonic activity in the Pine Island–Thwaites drainage system (Kaspari et al., 2004). These first accumulation rate histories in the ASE were limited primarily by the spatial extent of the radar data available to extend firn and ice-core accumulation chronologies, which are inherently point measurements, across the basin.

The collection of several high vertical resolution airborne radar datasets between 2009 and 2021 greatly expanded spatial coverage of radar data available to determine accumulation rates (Medley et al., 2013, 2014). Additional ice cores collected The Amundsen and Bellingshausen Sea sectors are also characterized by large interannual geopotential height variability (Connolley, 1997; Renwick, 2002; Lachlan-Cope and Connolley, 2006; Ding et al., 2012; Turner et al., 2013). The same mechanisms that combine to form the ASL also promote long-lived high pressure anticyclonic blocking systems (Sinclair, 1996; Renwick, 1998, 2005; R . Interannual blocking variability has been linked to marine air intrusion and accumulation variability recorded in the Roosevelt Island Ice Core, West Antarctica using automated weather stations (Emanuelsson et al., 2018); however, these processes are less well studied in the Amundsen Sea Embayment where coastal weather station observations of accumulation are limited (Lazzara et al., 2012). Deep and shallow ice cores in the ASE also provided more highly resolved accumulation records in locations with higher accumulation rates. In contrast to previous results, neither observed nor modeled accumulation rates showed any trend since 1980 (Medley et al., 2013). Hypsometric distributions of accumulation rates revealed gradients in accumulation that change with elevation and distance from the Antarctic coastline. These gradients were found to be smaller than those simulated in reanalysis products, especially on Thwaites Glacier (Medley et al., 2014). Medley et al. (2013, 2014) did not attempt to determine the cause of the accumulation hypsometry, perhaps due to a relatively short (thirty-year) and poorly resolved (roughly decadal) record to compare with atmospheric conditions in reanalysis products. They noted that further in-situ constraints from local, highly temporally resolved data may resolve discrepancies between modeled and observed accumulation rates (Medley et al., 2013). Although future advances in radar technology may enable retrieval of accumulation records with high temporal resolution deeper into the past, current highly-resolved radar-determined accumulation records in time and space are limited to roughly the past 40 years.

These methods rely on assumptions for snow deposition and densification and can convolve surface mass balance signals with integrated thinning and thickening signals associated with the settling and sintering of snow grains. Although these methods resolve annual and, more recently, seasonal changes in snowfall (Jones et al., 2023), they cannot determine relationships between accumulation eventsand atmospheric dynamics and moisture transport mechanisms that evolve on sub-seasonal timescalesregion, though well-suited to characterize West Antarctic accumulation variability on interannaul and longer timescales (Kaspari et al., 2004), cannot resolve individual snowfall events. Single snowfall events do not directly impact the long-term behavior of polar ice sheets, because each event represents only a small fraction of the integrated decadal to millennial surface mass balance forc-

ing required to ~~engage the intrinsic modes of~~ convey surface mass balance anomalies to the coast and drive marine outlet glacier ~~response (Christian et al., 2020; Robel et al., 2018). However, they~~ advance or retreat (Christian et al., 2020; Robel et al., 2018). Single snowfall events can be used to understand and link snowfall ~~events to understand~~ to moisture transport mechanisms that ~~change on longer timescales that are relevant for understanding the glacier's response to climate change and climate variability.~~ ~~This may be especially true in the ASE, where extreme precipitation events modeled in reanalysis account for more than half of the total precipitation (Maclennan and Lenaerts, 2021).~~

~~Recent work has suggested that extreme precipitation eventsmay be responsible for substantial accumulation on coastal portions of Thwaites Glacier (Maclennan et al., 2022b). Prior observational studies have focused on determining mean annual accumulation rates from firn cores and radar stratigraphy (). These studies have also hypothesized linkages to regional atmospheric conditions and suggested teleconnections to tropical Pacific variability; however, the records examined lack the temporal resolution to actually interrogate the mechanism responsible for accumulation, determine whether accumulation varies seasonally, and quantify the fraction of total precipitation associated with extreme precipitation events. Robust, high temporal resolution measurements of snow accumulation together with reanalysis data can elucidate relationships between accumulation and atmospheric conditions that could not be determined by past observations and linked modeling analyses~~represent the characteristic state of the atmosphere recorded in the snow deposited at the surface. By diagnosing composites of the atmosphere during precipitation events, we aim to increase understanding of the atmospheric dynamics that promote accumulation, particularly extreme accumulation (90th percentile of events) that represent the majority of accumulation in the ASE (Turner et al., 2019; Maclennan and .

1.1 ~~GNSS Interferometric Reflectometry~~

GNSS interferometric reflectometry (GNSS-IR) offers an exciting method to determine accumulation rates with high temporal resolution in remote and undersampled regions of the West Antarctic interior. ~~We divide this manscript into two parts. First, we focus directly on the GNSS data used in this study (Figure 1). We first introduce the GNSS sites and the GNSS interferometric reflectometry method. Then, we describe the inverse method used to infer accumulation rates from the reflector height time series and discuss the seasonality and extreme events expressed in this new record. In the second part of this manuscript, we relate the GNSS-IR time series to synoptic-scale meteorological conditions in the southern Pacific and their connection to tropical teleconnections. We first define and index extreme precipitation events observed in the GNSS-IR record. We then use the timing of these events to explore climate reanalyses to understand these highly localized records in the context of synoptic meteorology and planetary dynamics that promote precipitation in the region.~~

~~(A) Overview map of long-term GNSS-IR sites (LTHW in orange, KHLR in purple, and UTHW in blue), integrated vapor transport calculated between 300 hPa and 900 hPa pressure levels, the 500hPa geopotential height (contours), and an atmospheric river event detected on May 13, 2016. (B) Panels show the receiver position as a function of time. (C) Photo of the LTHW receiver and power system (credit: POLENET team). (D) Reflector height change in 2016 for all three long-term GNSS sites. Gray bars indicate the timing of atmospheric river events that made landfall in the ASE.~~

May 13, 2016
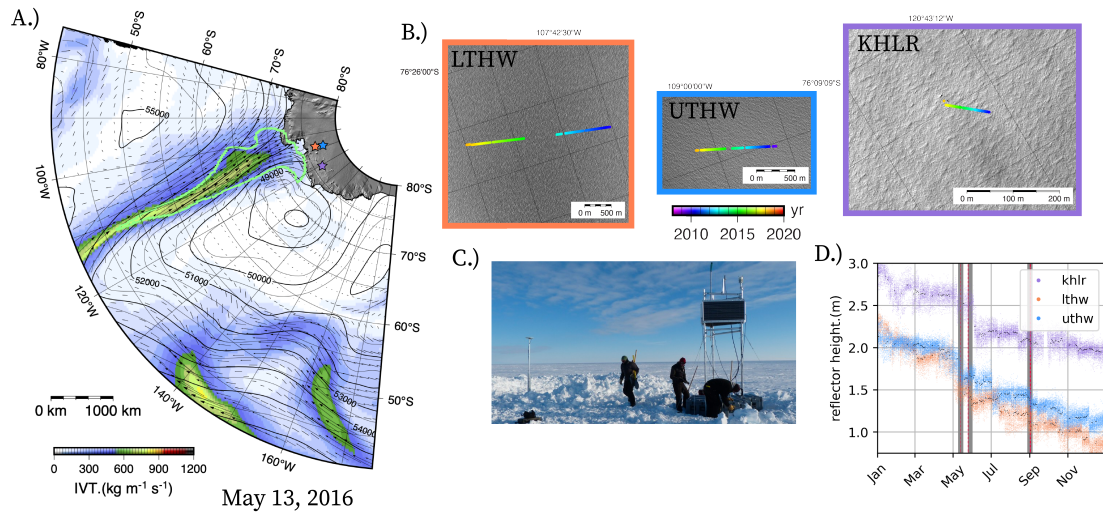
Figure 1. (A) Overview map of long-term GNSS-IR sites (LTHW in orange, KHLR in purple, and UTHW in blue), integrated vapor transport calculated between 300 hPa and 900 hPa pressure levels, the 500hPa geopotential height (contours), and an atmospheric river event detected on May 13, 2016. (B) Panels show the receiver position as a function of time. (C) Photo of the LTHW receiver and power system (credit: POLENET team). (D) Reflector height change in 2016 for all three long-term GNSS sites. Gray bars indicate the timing of atmospheric river events that made landfall in the ASE identified using methods described in the appendix corroborated by the catalog developed by Wille et al. (2021) .

160 ~~The Global Navigation Satellite System (GNSS)~~ GNSS positioning uses coded signals transmitted by GNSS ~~satellite constellations~~ satellites at different L-band frequencies to determine three-dimensional position estimates of GNSS receiver antenna locations. The timing of received GNSS signals provides range information important for establishing antenna positions~~but~~, but it is distorted by electromagnetic wave interactions with the neutral atmosphere, the ionosphere, and reflections off nearby surfaces before the wave reaches the antenna (i.e. ~~,~~ multipath reflections).

The distorted travel times associated with multipath reflections have conventionally been treated as noise and informed early
165 GNSS antenna gain pattern designs, which minimized multipath signals at high satellite elevation angles. ~~Larson et al. (2009, 2015)~~ Larson et al. (2009) established that multipath signals embedded in the signal-to-noise ratio (SNR) of GNSS positioning data contains useful information about the reflection surface geometry (i.e. ~~,~~ the height of the antenna above the surface) and the dielectric properties of the surface. Many subsequent studies have shown that the distance between the reflection interface and the antenna phase center can be calculated and monitored over time from the SNR recorded at the ~~receiver~~ GNSS antenna in order to
170 understand local surface evolution (Larson et al., 2015; Siegfried et al., 2017; Shean et al., 2017; Larson et al., 2020; Pinat et al., 2021) .

Despite the proven effectiveness of GNSS-IR methods to measure surface height and reflector amplitude changes associated with snow deposition~~(Shean et al., 2017; Larson et al., 2020; Pinat et al., 2021)~~, only two studies (Larson et al., 2015;

Siegfried et al., 2017) have used GNSS-IR to link surface height changes to ~~climate and~~ multi-year precipitation ~~variability on~~
~~the~~ and climate variability on ice sheets. This is largely due to ~~challenges maintaining~~ the logistical challenges associated with supporting multi-year on-ice GNSS receiver networks~~that have traditionally been deployed as part of short-duration arrays~~, where stations must be raised regularly (every 1-3 years) to prevent burial due to snow accumulation. Over the past fifteen years, ~~The~~ GNSS receivers located in the ASE (Figure 1, 2) have been maintained to support several different projects that investigate solid Earth deformation (e.g. Hansen et al., 2023), glacial isostatic adjustment (e.g. Barletta et al., 2018), and ice flow ~~(Figure 1, 2). More~~ (e.g. Hoffman et al., 2020). Through the application of GNSS-IR, more than ten years of nearly continuous GNSS operation also offers a unique opportunity to explore atmospheric dynamics that promote and control precipitation and accumulation in the ASE.

We use GNSS-IR SNR data from three long-term sites: lower Thwaites Glacier (LTHW), upper Thwaites Glacier (UTHW), and Kohler Glacier (KHLR), as well as GNSS campaign arrays that were deployed across Thwaites Glacier as part of geophysical surveys in the austral summers of 2007-2008 ~~,~~ and 2008-2009 ~~, and 2009-2010~~ to link extreme precipitation events and synoptic-scale atmospheric rivers observed in reanalysis to highly localized accumulation records at individual GNSS sites (Figure 1, 2). Using our unique GNSS-IR records, we quantify the seasonal cycle of precipitation and elevation dependence of accumulation in the ASE. We also verify that extreme precipitation events supply the majority of total accumulation in the ASE. We then use the GNSS-IR records of extreme accumulation events to composite near-surface temperature, atmospheric pressure and integrated vapor moisture transport simulated in reanalysis in order to better understand the drivers of extreme precipitation in the ASE. We use these composites to understand the synoptic conditions and global teleconnections that promote extreme snowfall in the ASE. Our results suggest that extreme snowfall events observed in the ASE are coincident with blocking conditions in the Bellingshausen Sea.

2   ~~Part 1: From~~ GNSS ~~reflector heights to accumulation time series~~interferometric reflectometry

2.1   ~~Methods: GNSS interferometric reflectometry reflector heights~~

~~The reflector~~ Here we report on multi-year deployments for three on-ice GNSS sites in West Antarctica's Amundsen Sea Embayment: two along the trunk of Thwaites Glacier (upper Thwaites, UTHW, and lower Thwaites, LTHW) and one on nearby Kohler Glacier (KHLR). The UTHW site was deployed in the 2008-2009 austral summer. The LTHW and KHLR sites were deployed in the 2009-2010 austral summer. Although there are intermittent data gaps due to power loss, all three sites have been regularly maintained and remain active today. In addition to the long-term sites, we also apply GNSS-IR to GNSS sites that were deployed on Thwaites Glacier during the 2007-2008 and 2009-2009 austral summers. During the 2007-2008 and 2008-2009 austral summers, 17 sites were deployed along two flowlines, which aimed to measure short-timescale (minutes to days) ice-velocity fluctuations from the coast towards the West Antarctic Ice Sheet central ice divide and Bentley Subglacial Trough. When possible, GNSS monuments installed in the 2007-2008 austral summer were reoccupied in the 2008-2009 austral summer; if a monument could not be found, the GNSS site was deployed at the position of the 2007-2008 monument as calculated from satellite ice-velocity data (Joughin et al., 2009). The array in 2007-2008 array was operational in January

2008. The 2008-2009 array was operational in December 2008 and January 2009. All GNSS site locations are plotted in Figure 2a.

Reflector height time series ~~are~~ were calculated using the workflow described by Roesler and Larson (2018), which is based

210   on the earlier work of Larson et al. (2015). Daily solutions for receiver position were calculated kinematically relative to the sites of nearby base stations (TF01 ~~for the campaign~~ and WAIS for the campaign sites; ~~BACK and HOWN for~~ permanent GNSS sites at Backer Island and Howard Island for the long-term sites) using differential carrier-phase positioning estimates from the ~~track~~ Track software (Chen, 1998; King, 2004; Hoffman et al., 2020). Daily-averaged position solutions for the base station sites were determined in GAMIT/GLOBK following standard GNSS processing methods for glaciological applications

215   (King, 2004). The reflector height was calculated from the signal-to-noise ratio (SNR) data assuming a planar reflector surface geometry. After direct signal effects are removed, the SNR data for a single satellite and receiver can be modeled as

$$SNR(e) = A(e) \sin \left(\frac{4\pi H_R}{\lambda} \sin(e) + \phi \right),$$ (1)

where A is the amplitude, which depends on the transmitted GNSS signal power, the satellite elevation angle above the horizon, the surface dielectric constant and its roughness, H_R is the reflector height, λ is the wavelength of the transmitted GNSS signal, and ϕ is a phase constant. This representation means a periodogram can be used to estimate H_R from the

220   dominant frequency:

$$f = \frac{2H_R}{\lambda}.$$ (2)

To resolve this frequency, the antenna must be at least two wavelengths above the surface ($0.4 - 0.5$ m, for GPS L1 and L2 frequencies). The elevation and azimuth angles ~~are~~ were calculated from the broadcast GPS ephemeris. The dominant SNR frequency ~~is~~ was determined using a ~~Lomb Scargle~~ Lomb-Scargle periodogram. On average, this results in ~~70~~ $\sim$ 70 estimates of SNR frequency every day, which can be related to reflector height using ~~equation~~ Equation 2.

225   We ~~eliminate~~ eliminated weak signals for each time increment that are 0.3 m from the median reflector height for that time increment. Longer sample intervals for calculating reflector heights provide a more robust result due to the larger number of samples in the increment. For the long-term sites, ~~dense temporal sampling is not advantageous to spatially track snow accumulation due to sparse spatial sampling, so we use daily increments. The~~ we used daily averaged reflector heights to determine daily accumulation rates. See Supplement Table S1 for a chart detailing the days when we have snowfall observations

230   from GNSS with previous observations from acoustic depth gauges available from the Automatic Weather Station Project (Lazzara et al., 2012). We used 3-hour ~~increment was chosen to understand and estimate~~ estimates of reflector height to snow accumulation moving across the campaign GNSS array~~as storms~~, because station spacing was sufficient to map storms that moved up Thwaites Glacier ~~. We then use the~~ (Figure 7, Supplemental movie). The mean and standard deviation of the filtered signals (level 2 product shown in Figures 2 ~~, 3)~~ and 3) were used to derive accumulation records (level 3 product shown in

235   Figure 5) ~~, which we describe in full in the next~~ using the inverse method described in the following section.
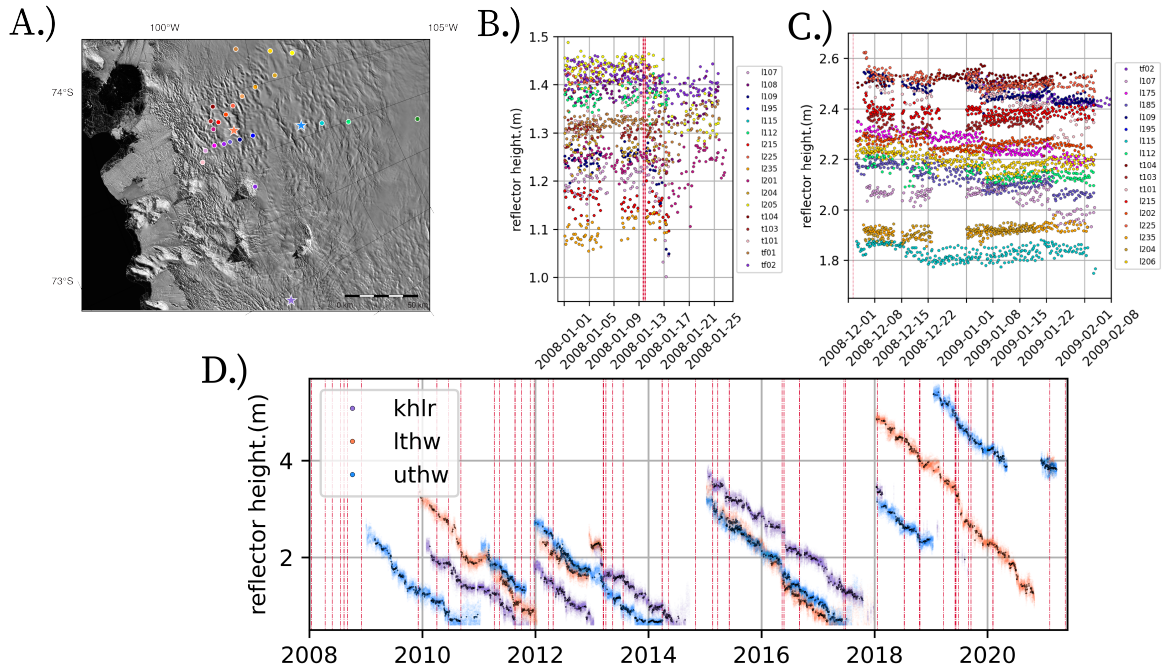
Figure 2. (A) Locations of all the GNSS sites (long-term sites indicated with stars and campaign sites indicated with circles) with reflector height observations from the (B) 2007-2008 array, (C) the 2008-2009 array, and (D) the long-term GNSS sites. For the long-term records, all reflection heights are shown with daily median reflectors in bold. Atmospheric river events are marked with red vertical dashed bands (see ~~appendix section~~ Appendix Section A2 for more details on event detection methods).

2.0.1 ~~Methods: Accumulation and densification forward model~~

2.1 Methods: Accumulation and densification forward model

To determine the accumulation record from observations of reflector height, we use an inverse method (Metropolis-Hastings algorithm) that requires a forward model that translates the parameters of interest (in our case, an accumulation and densification time series) into observables (reflector height time series). Our forward reflector height model for on-ice GNSS sites represents one-dimensional multi-layer snow compaction and grain settling from the surface to the depth of the GNSS antenna monument base. Each snow layer in the model is described by its thickness and density. Layers evolve following the compaction constitutive relation:

$$\frac{\partial \epsilon_i}{\partial t} = -\frac{\sigma_i}{\eta}, \tag{3}$$

where ϵ_i is the layer strain, η is the snow viscosity, and σ_i is the overburden stress of the layers above. The vertical stress of the overlying layers is computed for each layer, i, as
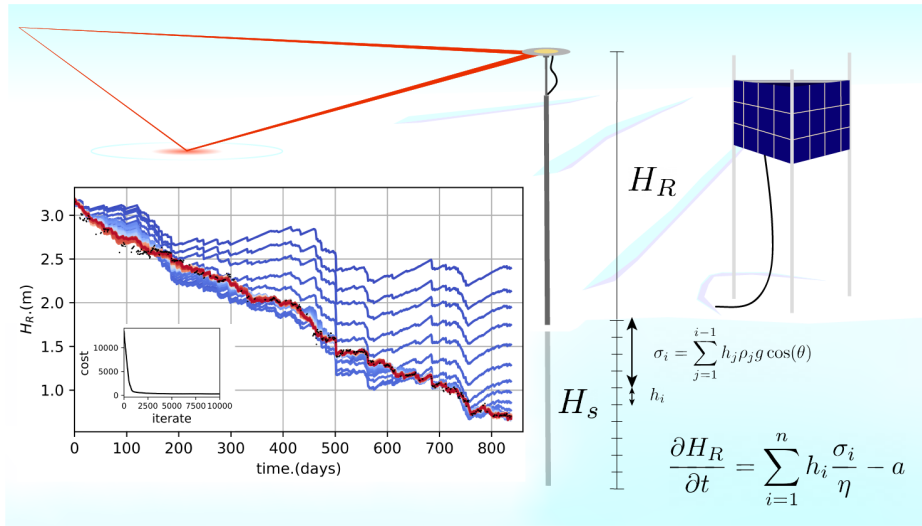
Figure 3. ~~Model~~ The model schematic ~~along with the~~ and convergence pattern of the Metropolis-Hastings algorithm used to produce an accumulation time series. In the main plot, we show the convergence of the modeled RH (colored lines) and the observed reflector height time series (black points) as a function of model iterate. The objective function we use to score solutions is shown as an inset plot. The misfit of the model compared to observations decreases and converges as a function of iteration in the inverse procedure.

$$\sigma_i = \sum_1^{i-1} g \rho_i h_i \cos(\theta), \tag{4}$$

where θ is the local surface slope, g is the terrestrial gravitational constant, and ρ_i and h_i are the layer density and thickness, respectively. The snow viscosity, η, which describes how efficiently stress is transmitted through the column, has been linked to snow temperature, liquid water content, and snow grain geometry. Without in-situ observations of snow properties, we fix the viscosity for the duration of each reflector height experiment.

250   **2.1.1**   ~~**Methods: Reflector height inverse method**~~

2.2   **Methods: Reflector height inverse method**

The number of unknown parameters in our model scales with the length of the reflector height record. We reset the inference of accumulation, viscosity, and initial snow density each time the antenna mast is raised (quasi-annually). We use Bayes' theorem to compute the distributions of accumulation at each time step and specify a likelihood model, assuming that observations

255   of reflector height are independent in time and normally distributed around the true value at each data point with variance $\sigma_{R_{h_{obs_k}}}$. The objective functional defined by the least-squares difference between observed, $R_{h_{out_k}}$, and modeled, $R_{h_{obs_k}}$, reflector heights for each increment, k, in the time series when observations are available is described by

$$\phi_k(m_k) = (R_{h_{out_k}}(m_k) - R_{h_{obs_k}})^2_{,.}$$ (5)

~~which we use~~ We use this objective functional to define the likelihood of the modeled reflector heights, given the observations:

$$p(R_{h_{obs}}|m) \propto \prod_{k \in n} \exp\left(\frac{-B\phi(m_k)}{\sigma^2_{R_{h_{obs_k}}}}\right).$$ (6)

260   The priors for the accumulation record are modeled with Gaussian distributions with parameters listed in Supplementary Table ~~S1~~S3. The Gaussian distributions for the snow accumulation are centered on an initial estimate of mean snow accumulation that takes the maximum of the difference of snow surface height divided by the mean snow density (300 kg/m^3) and a prior of no snowfall $(300 \cdot \max(R_{h_{obs_{k+1}}} - R_{h_{obs_k}}, 0))$. With a likelihood model and a prior estimate of the model parameters, we use Monte Carlo methods to sample and thereby estimate the posterior distribution of the accumulation, density, and snow

265 viscosity, and evaluate the statistical properties of the samples as a proxy for the joint posterior distribution of the model parameters. We use the Metropolis-Hastings algorithm to build estimates of the posterior distribution, map model degeneracy, and understand parameter uncertainty. The Metropolis-Hastings algorithm samples the prior estimate of each model parameter and independently updates each parameter at each iteration by randomly drawing a sample from the proposed distribution. If the sampled posterior probability is greater for the proposed distribution than the current distribution, the new parameter value

270 is accepted. Otherwise, it is accepted with probability (P_{accept}) proportional to the ratio of the current probability $(p(m_i))$ and that of the proposed value $(p(m_{i+1}))$.

$$P_{\text{accept}} = \min\left(1, \frac{p(m_{i+1})}{p(m_i)}\right)$$ (7)

$$P_{\text{accept}} = \min\left(1, \frac{A\exp(-B\phi(m_{i+1}))}{A\exp(-B\phi(m_k))}\right) = \min(1, \exp(-B(\phi(m_{k+1}) - \phi(m_k))))$$ (8)

    Here B is a tunable regularization parameter to facilitate convergence. We ~~present the initial results of the time series below. Then, in Part 2, we~~ use these time series to explore possible drivers of precipitation ~~phenomena~~ by connecting the events we observed ~~to extreme precipitation in reanalysis.~~

275 **2.2.1**   ~~**Results: GNSS-IR accumulation time series**~~

~~Using~~ using GNSS-IR ~~, we create the first 10-year time series of snow accumulation at three sites in one of the most remote areas of West Antarctica: the Amundsen Sea Embayment. Currently, all precipitation on Thwaites at the sites of the GNSS receivers falls as snowfall with no discernible rain events in the interior locations of the GNSS recorded in reanalysis. On~~

Thwaites, precipitation is most frequent and intense in the austral winter (June, July, & August; JJA) with a peak accumulation in August that tapers into the austral summer to a minimum in January (Figure 6). At LTHW, precipitation is ~50% higher in austral winter than in austral summer. The seasonal signal is more muted at UTHW, with only a ~30% difference between seasons. At the Kohler Glacier GNSS station (KHLR), peak accumulation occurs in March and is minimum in November. Interannual variability and the seasonal cycle are driven primarily by changes in the frequency of extreme precipitation events. Following, (Maclennan and Lenaerts, 2021), we define extreme precipitation events using the 90th percentile threshold. Extreme events account for over half the total accumulation at all GNSS sites and explain 80% of the snow accumulation variability in reanalysis. These events also change seasonally (Figure 6). Over the observation time period (2009-2020), 13% of wintertime days (96 days), 6.2% of summertime days (45 days), 10.4% of springtime days (71 days), and 10.2% of fall days (82 days) experience extreme precipitation. to extreme precipitation events in reanalysis.

Observed cumulative accumulation at the LTHW, UTHW, and KHLR receiver sites with all atmospheric river events (dashed red vertical lines) and the events that occur within 2 days of the 90th percentile of daily accumulation rates (gray vertical lines). (A) Interannual accumulation and seasonal cycle across the lower Thwaites, upper Thwaites, and Kohler GNSS sites. (B) Distribution of the difference between seasonally high accumulation event frequency and low accumulation event frequency at upper and lower Thwaites (DJF-JJA) and Kohler Glacier (SON-MAM).

Using the short-duration GNSS array with the two long-term Thwaites sites that were maintained for 1 month in the 2007-2008 austral summer and two months in the 2008-2009 austral summers, we also document the spatial patterns of snowfall across 20 stations in the ASE (Figure 2). During these shorter-duration campaigns, we observed 7 extreme precipitation events during the two summers (Figure 7). Across the short-term arrays in both summers, we find that it snows 2-4x more on lower Thwaites (800 m elevation) than in the higher elevation sites (1200 m elevation) during extreme events (Figure 7). Gradients in accumulation are less strong on days when we do not observe extreme events. In the following section, we investigate the character of these extreme events and potential drivers with reanalysis. (A) The guiding 500h Pa geopotential height (contours) and the integrated vapor transport for the 2007-2008 array atmospheric river event with the cumulative accumulation at the site of each receiver for the (B) 2007-2008 and (C) 2008-2009 seasons of array data. Average daily snowfall as a function of elevation for (D) the 2007-2008 and (E) the 2008-2009 austral summers.

3   Part 2: From extreme accumulation event detection to validation and event characterization in reanalysis

The remainder of this study is guided by two connected goals:

1. To test and further understand hypotheses that have been drawn from reanalysis alone without the aid of long-term GNSS-IR observations of snow accumulation. Specifically, we seek to verify recent studies that have found a strong seasonal cycle in annual snowfall in West Antarctica and studies that have identified extreme precipitation as a major fraction of total precipitation in the ASE (Maclennan and Lenaerts, 2021; Maclennan et al., 2022a).

 2. ~~To use our unique 10-year accumulation record to inform seasonal composites of pressure, surface temperature, and wind anomalies preceding extreme precipitation events on Thwaites Glacier and evaluate the importance of blocking and tropical teleconnections on extreme precipitation in the ASE.~~

2.1 ~~Data: Reanalysis~~

~~Due to the spatial and temporal limitations of in-situ observations available for the Southern Ocean and the WAIS, reanalysisproducts have been essential for examining spatial patterns and trends in atmospheric pressure, temperature, and moisture transport in Antarctica. Reanalysis has helped identify the Amundsen Sea Low (ASL), a quasi-stationary climatological low-pressure system revealed in monthly average pressure anomalies located between the Antarctic Peninsula and the Ross Sea (Hosking et al., 2013). The ASL is one of three low-pressure systems distributed along the circumpolar trough (Turner et al., 2013) and moves through the sector with the highest variability circulation in the Southern Hemisphere (Lachlan-Cope et al., 2001). The ASL also exhibits a pronounced seasonal cycle in location and depth (the geopotential height of the 1000hPa pressure level Fogt et al., 2012; Ho that has been hypothesized to drive seasonal changes in moisture transport to the Antarctic interior. On average, the ASL depth is greatest during austral winter and weakest during the austral summer (Hosking et al., 2013). The center of the ASL also changes location seasonally, tending to be located farther northward and westward in austral summer and more southward and eastward in austral winter (Fogt et al., 2012; Hosking et al., 2013; Turner et al., 2013). The climate of West Antarctica and especially West Antarctic precipitation has been found to be very sensitive to changes in the ASL (Raphael et al., 2016; Turner et al., 2013; H . Because the low-frequency variability in ASL behavior has been connected to the low-frequency surface mass balance (Raphael et al., 2016; Turner et al., 2013; Hosking et al., 2013), understanding the drivers of multi-year variability and the dynamics of the ASL is important for understanding the committed response of rapidly changing outlet glaciers, such as Thwaites Glacier (Robel et al., 2018; Christian et al., 2020). This requires developing a deeper understanding of the synoptic and sub-synoptic scale cyclonic systems that propagate through the Amundsen region and average together over time to form the low-pressure anomaly (Fogt et al., 2012).~~

~~Following many of the studiescited above~~

2.1 Methods: Reanalysis composites

Following many previous studies, we use MERRA-2, RACMO2, and ERA5 reanalysis products to contextualize our observations of local surface height change from GNSS with large-scale circulation ~~(Gelaro et al., 2017; van Wessem et al., 2018; Hersbach et al., 2~~ . ~~These products generally agree with one another; however, they all underestimate the frequency of extreme events compared to the events recorded in the GNSS-IR records (Supplementary Figure S1). They are also poorly correlated with the GNSS-IR records (Supplementary Figure S1D, E, F).~~ (Gelaro et al., 2017; van Wessem et al., 2018; Hersbach et al., 2020). We chose to focus on ERA5 ~~as simulated~~ because past studies have shown that observed snow accumulation from ~~ERA5 agreed~~ GNSS-IR agreed better with ERA5 snow accumulation records than with ~~measured snow accumulation more than~~ MERRA-2 ~~,~~ and RACMO2 ~~(Supplementary Figure S1).~~

snow accumulation records (Maclennan et al., 2022a, Supplementary Figure S1, Supplementary Table S3.). ERA5 is the newest global atmospheric reanalysis product from the European Centre for Medium-range Weather Forecasts (ECMWF) and has 0.25° latitude (28 km) by 0.25° longitude (~ 7 km^2) resolution (Hersbach et al., 2020). We focus our study on the Southern Pacific but include reanalysis data from tropical latitudes (20° N to 90° S) to evaluate the possibility of tropical teleconnections that have been suggested to affect precipitation variability in accumulation records preserved in firn and ice cores.

The detected atmospheric rivers with the guiding 500 hPa geopotential height and the integrated vapor transport for the events that occur within three days of the 95th percentile of height changes observed with GNSS-IR.

2.2 ~~Methods: Reanalysis composites~~

Using the GNSS-IR time series, extreme precipitation was classified using a seasonally corrected 90$^{\text{th}}$ percentile threshold of daily accumulation rates for the lower Thwaites and upper Thwaites sites accumulation events. The union of these two indices was used to create a Thwaites Glacier catchment extreme accumulation event dataset. The results ~~with Kohler~~ do not change substantially when the Kohler Glacier site included in this index ~~do not change substantially~~; however, because of the observed offset in the accumulation seasonality, we exclude Kohler from the merged index of the sites on Thwaites Glacier. The GNSS-IR catalog of extreme accumulation events was used to calculate composite maps of geopotential height and wind anomalies at the 500 hPa pressure level, blocking anomalies calculated from anomalies of geopotential height at the same pressure level, surface temperature anomalies (2 m), near-surface wind anomalies (10 m), integrated vapor moisture (IVT) transport anomalies, and Rossby source anomalies using ERA5 daily averages. Rossby source anomalies were calculated from 200 hPa winds following the methods described by (Trenberth et al., 1998) and (Holton, 2004), as implemented by (Dawson, 2016, Supplementary Figures S6, S7). Daily average outgoing longwave radiation (OLR) anomaly composites and sea surface temperature anomalies were calculated from NOAA SST data and OLR satellite data (Figure 11, Supplementary Figures S2, S4, and S5; Liebmann and Smith, 1996). Composites were calculated for the ten days preceding the onset of extreme precipitation and corrected for anomalies calculated relative to seasonal mean conditions. The interval of ten days was chosen to evaluate the importance of both proximal atmospheric dynamics near the Amundsen Sea and tropical and extratropical teleconnections that precede changes in the ASE by ~~days to weeks~~ up to ten days (Li et al., 2015, 2021). As part of this analysis, we also built catalogs of blocking events and the atmospheric rivers that made landfall in the ASE, both of which have been connected to extreme precipitation and changes in the surface elevation of the West Antarctic ~~ice sheet~~ Ice Sheet (Adusumilli et al., 2021). More information on the methods used to create these catalogs can be found in ~~the appendix (Appendix section~~ Appendix Section A1~~)~~.

2.1.1 Results: GNSS-IR accumulation time series

Using GNSS-IR, we created the first $\sim$ 10-year time series of snow accumulation at three sites in one of the most remote areas of West Antarctica: the Amundsen Sea Embayment. Currently, all precipitation on Thwaites Glacier at the GNSS sites falls as snow with no discernible rain events recorded in reanalysis or GNSS-IR surface reflection amplitude. On Thwaites, precipitation is most frequent and intense in the austral winter (June, July, & August; JJA) with peak accumulation in August
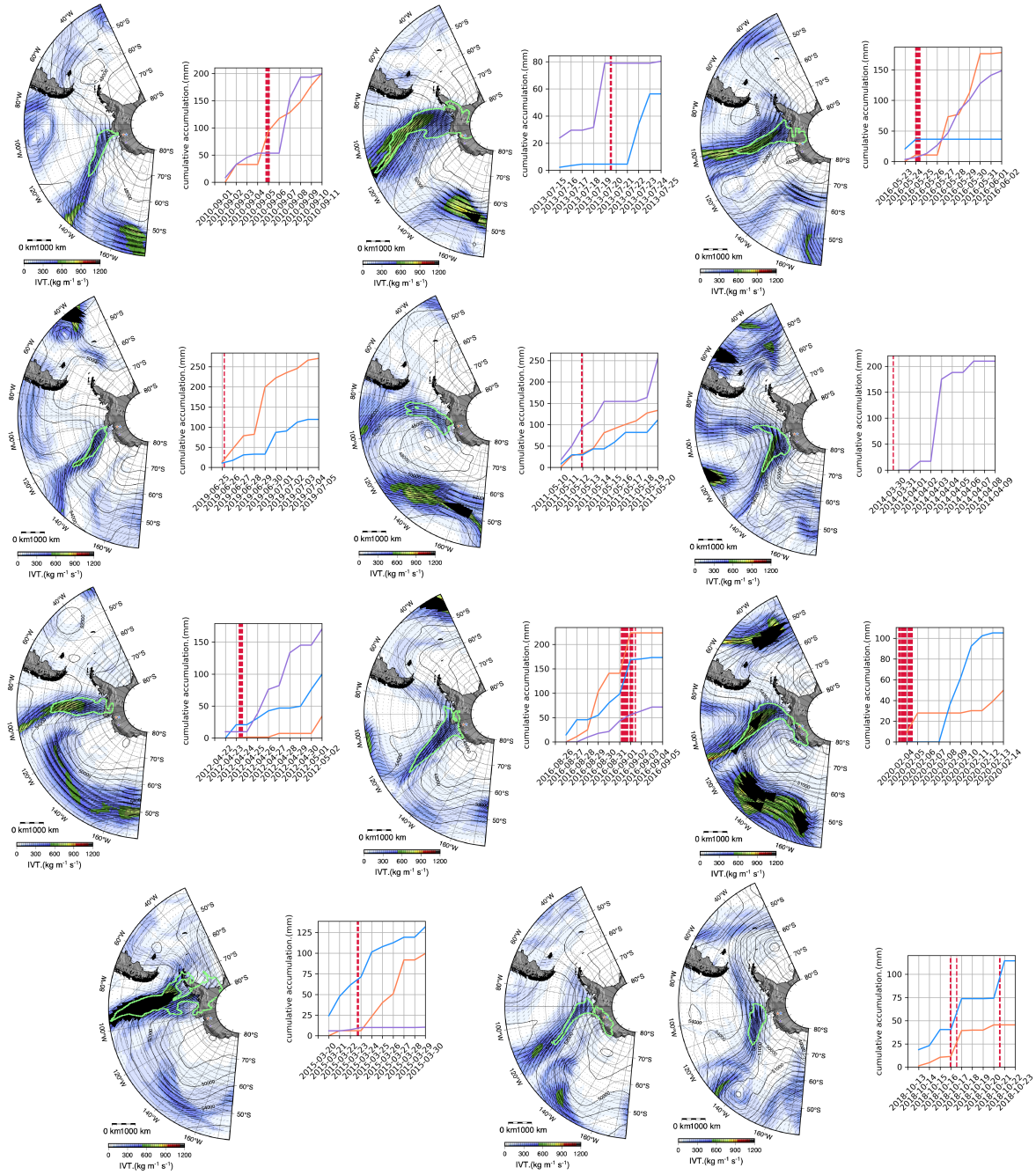
Figure 4. The detected atmospheric rivers (Cyan green outlines) with the guiding 500 hPa geopotential height (contours) and the integrated vapor transport for the events (colormap) that occur within three days of the 95th percentile of height changes observed with GNSS-IR.
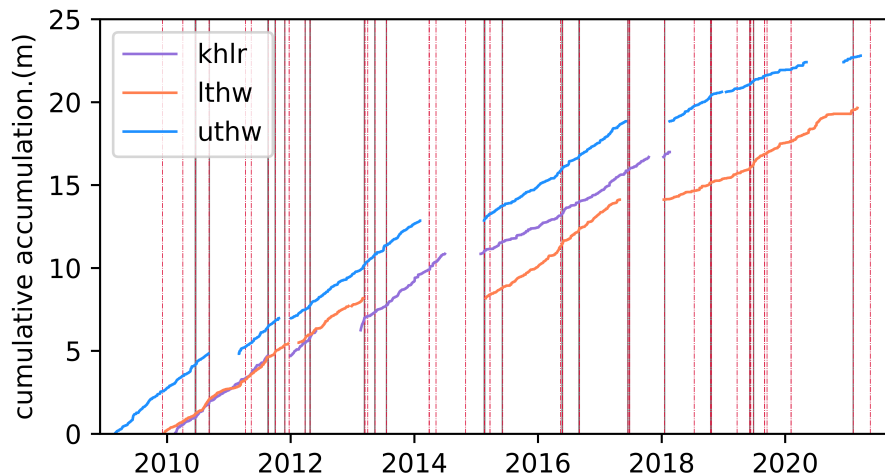
Figure 5. Observed cumulative accumulation at the LTHW, UTHW, and KHLR receiver sites with the timing of atmospheric river events that made landfall in the ASE (dashed red vertical lines) and the extreme accumulation events measured with GNSS-IR that occur within two days of the atmospheric river events (gray vertical lines).

375   that tapers into the austral summer to a minimum in January (Figure 6). At LTHW, precipitation is ∼50% higher in austral winter than in austral summer. The seasonal signal is more muted at UTHW, with only a ∼30% difference between seasons. At the Kohler Glacier GNSS station (KHLR), peak accumulation occurs in March and is minimum in November. The interannual variability and the seasonal cycle are driven primarily by changes in the frequency of extreme precipitation events. Extreme events account for over half the total accumulation at all three long-term GNSS sites and explain 80% of the snow accumulation

380   variability in reanalysis. These events also change seasonally (Figure 6). Over the observation time period (2009-2020), extreme precipitation events occur on 13% of wintertime days (96 days), 6.2% of summertime days (45 days), 10.4% of springtime days (71 days), and 10.2% of fall days (82 days).

    Using the short-duration GNSS arrays that were deployed for one month in the 2007-2008 austral summer and two months in the 2008-2009 austral summers, we also document the distributed patterns of snowfall across 17 stations in the ASE (Figure

385   2). During these short-duration campaigns, we observed seven extreme precipitation events during these two summers (Figure 7). Across the short-term arrays in both summers, we find that it snows 2-4 times more at lower Thwaites (800 m elevation) than in the higher elevation regions of the catchment (1200 m elevation) during extreme events (Figure 7). Elevation gradients in accumulation are less strong on days when we do not observe extreme events.
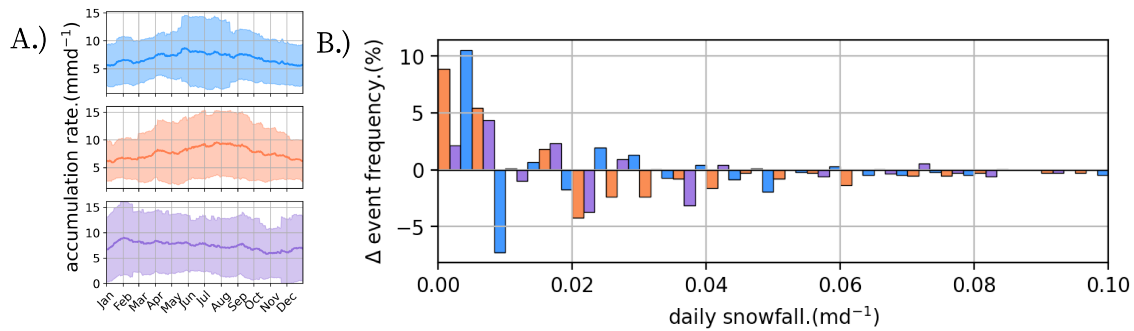
Figure 6. (A) Interannual accumulation and the seasonal accumulation cycle at the lower Thwaites, upper Thwaites, and Kohler GNSS sites. (B) Distribution of the difference between seasonally high accumulation event frequency and low accumulation event frequency at upper and lower Thwaites Glacier (DJF-JJA) and Kohler Glacier (SON-MAM).
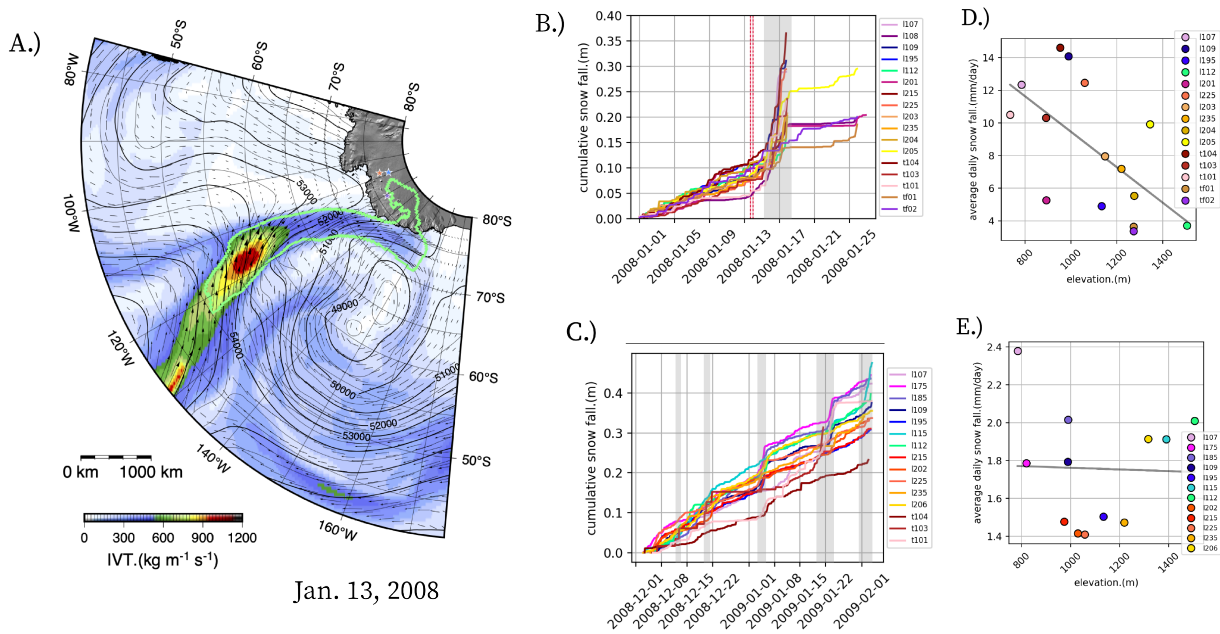
Figure 7. (A) The guiding 500 hPa geopotential height (contours) and the integrated vapor transport for the 2007-2008 array atmospheric river event with the cumulative accumulation at the site of each receiver deployed as part of the (B) 2007-2008 and (C) 2008-2009 GNSS arrays. Red lines indicate timing of atmospheric rivers that make landfall in the ASE. Gray shading indicates timing and duration of extreme precipitation events determined from all array GNSS sites. Average daily snowfall as a function of elevation for (D) the 2007-2008 and (E) the 2008-2009 austral summers.

2.2 Results: Composite investigation of reanalysis

2.2.1 Summer and winter time blocking in the Amundsen and Bellingshausen ~~Sea~~Seas

The mean blocking conditions from the days preceding the onset of observed extreme accumulation at the GNSS sites for summer (DJF) and winter (JJA) events are illustrated in Figure 8. We found that between two days prior to (day -2) and the onset of snowfall (day 0) ~~,~~ blocking is present in the ~~Bellinghausen and Amundsen Sea~~ Bellingshausen and Amundsen Seas (defined by bounds $55°$S, $75°$S, $120°$W, and $45°$W) during 42% of winter extreme precipitation events and 37% of summer extreme precipitation events. Snowfall events with atmospheric blocking also have statistically higher mean precipitation rates than those without blocking.

The blocking frequency anomalies associated with both summer and wintertime extreme precipitation events reveal significant blocking of the westerly flow in the ~~Bellinghausen~~ Bellingshausen and Amundsen Seas before and during extreme snowfall events (Figure 8). The composites of 500 hPa winds are also consistent with blocking over large areas of the ~~Bellinghausen~~ Bellingshausen Sea during extreme snowfall events. During the summer extreme precipitation events, blocking frequency anomalies are higher (note the difference in color scale) compared to wintertime blocking anomalies associated with extreme wintertime precipitation (Figure 8). Austral summer blocking anomalies also cover a significantly larger area than the austral winter anomalies and extend westward to much of the Amundsen Sea. In the austral winter, anomalously negative blocking frequency is observed closer to the Thwaites Glacier catchment. This low-pressure austral winter anomaly drives anonymous northerly mid-level winds that impinge on the coast of West Antarctica and appear to strengthen along the eastern flank of the anticyclone.

The mean blocking frequency (2009-2020, Figure 10) across all seasons in the Southern Ocean is largest in the Amundsen and ~~Bellinghausen~~ Bellingshausen Seas. Blocking frequency in this region increases and shifts zonally from the Amundsen Sea in the summer to the ~~Bellinghausen~~ Bellingshausen Sea in the winter. The amplitude of blocking frequency change also increases with a maximum in winter and a minimum in the preceding fall. The blocking frequency anomalies associated with extreme accumulation events over the period of observations are highest during summer and spring when the total frequency of blocking is low. This clear pattern in blocking frequency anomaly suggests that blocking of moist mid-latitude westerly flow north of the Amundsen and ~~Bellinghausen~~ Bellingshausen Seas in summer and spring drives significant summer and spring precipitation. In the next section, we use composites of near-surface temperature and integrated vapor moisture transport to explore these relationships further.

2.2.2 Summer and winter time vapor transport in the Amundsen Sea

The mean surface temperature and vapor transport conditions on the days preceding the onset of ~~observed~~ extreme precipitation events we observe with GNSS-IR are illustrated in Figure 9. Positive near-surface temperature anomalies are present across the Amundsen Sea and the southern Pacific two days before extreme precipitation is observed on Thwaites Glacier. These temperatures steadily increase and peak on the day of the extreme event with positive temperature anomalies exceeding $1.5°$ C (Figure 9). During austral summer (DJF), these near-surface temperature and wind anomalies appear to come from the

Summer blocking preceding Extreme Snowfall   Winter blocking preceding Extreme Snowfall
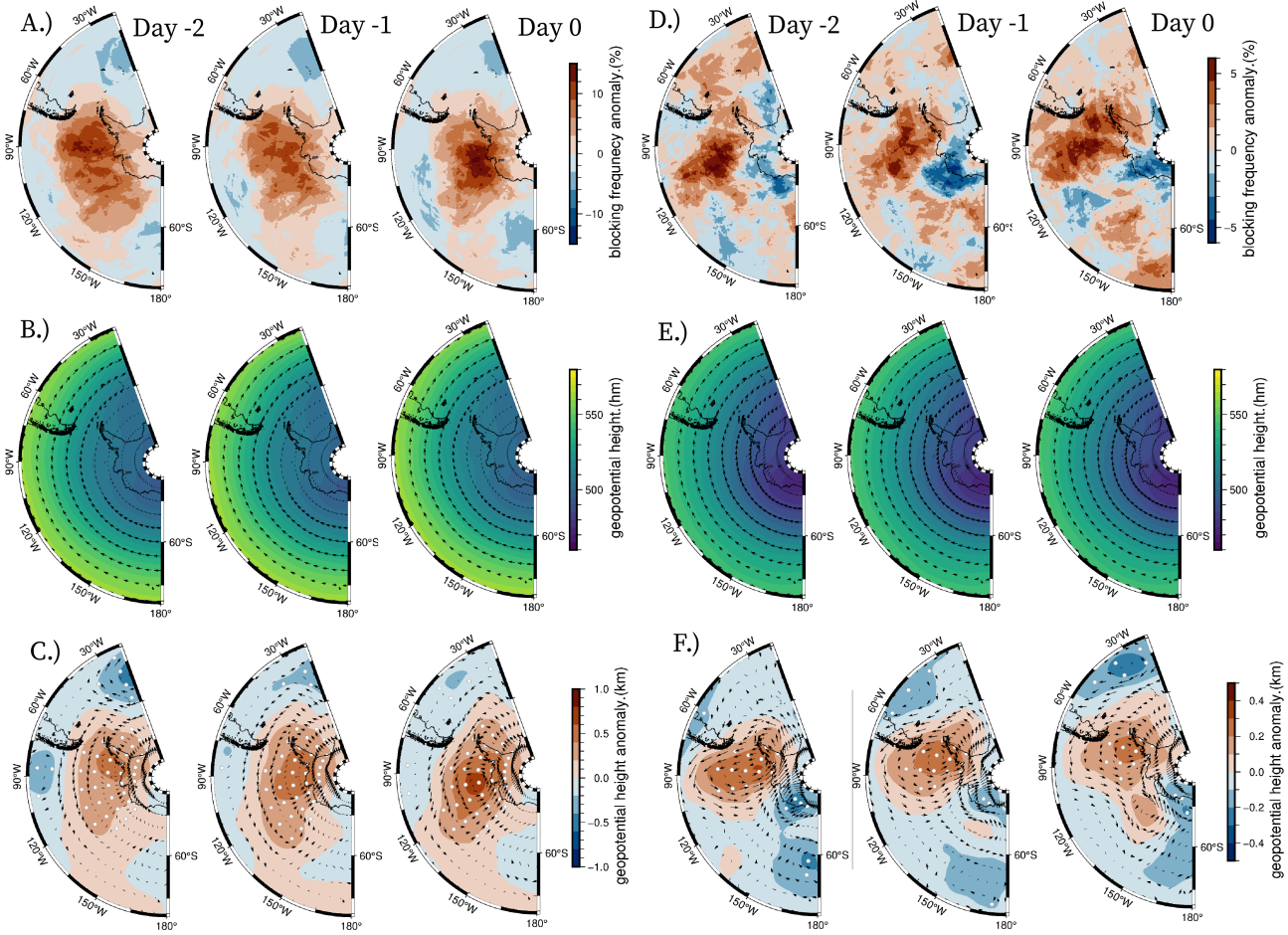
Figure 8. (A) ~~blocking~~ Blocking frequency anomaly, (B)500 hPa geopotential height shown with vectors of the 500 hPa winds, and (C) 500 hPa geopotential height anomaly and wind anomaly for extreme precipitation events observed during the austral summer (DJF). (D) ~~blocking~~ Blocking frequency anomaly, (E) 500 hPa geopotential height and winds, and (F) 500 hPa geopotential height and wind anomaly observed during the austral winter (JJA). The day indices are relative to the day of precipitation onset at the GNSS receivers. Stippling of anomalies indicates significance at 95% confidence.

northwest. During the austral winter (JJA), anomalously high near-surface temperatures increase in the Amundsen Sea from the northeast (Figure 9A, D).

425   The mean integrated vapor transport (IVT) associated with these events also shows enhanced values in the Amundsen and Ross Seas. The circum-Antarctic jet that transports the majority of high latitude moisture in the Southern Hemisphere is diverted southward expressed as a negative easterly IVT anomaly where IVT is highest (Figure 9B, E, C, F). This negative moisture anomaly is coherent with a positive westerly and northerly IVT anomaly at higher latitudes that extends into the

Figure 9. (A) ~~near-surface 500hPa geopotential height~~ Near-surface (2 m) temperature anomaly, (B) mean integrated vapor moisture transport, and (C) integrated moisture transport anomaly for extreme precipitation events during the austral summer (DJF)~~precipitation events on Thwaites,~~. (BD) ~~geopotential height~~Near-surface temperature anomaly~~calculated relative to 30-day rolling~~, (E) mean integrated vapor moisture transport, and (CF) ~~blocking frequency~~integrated vapor moisture transport anomaly for extreme precipitation events during the austral winter (JJA). The day indices are relative to the day of precipitation onset at the GNSS receivers. Stippling of anomalies ~~in (A)~~ indicates significance at 95% confidence.

West Antarctic interior (Figure 9C, F). In austral summer, the positive IVT anomalies are more uniform and diverted to higher latitudes by similarly uniform negative westward IVT anomalies. In austral winter, IVT anomalies integrated over the area of the entire Pacific are stronger than in austral summer; however, the spatial structure of the anomalies is more heterogeneous and insignificant at 95% confidence.

Atmospheric river event frequency also varies seasonally with larger events making landfall in austral winter months. These events make up only a small fraction of the extreme events that appear to control precipitation on Thwaites. Similar to the conclusions of other studies ~~(i.e., Maclennan and Lenaerts, 2021)~~(i.e. Maclennan and Lenaerts, 2021), we find that atmospheric
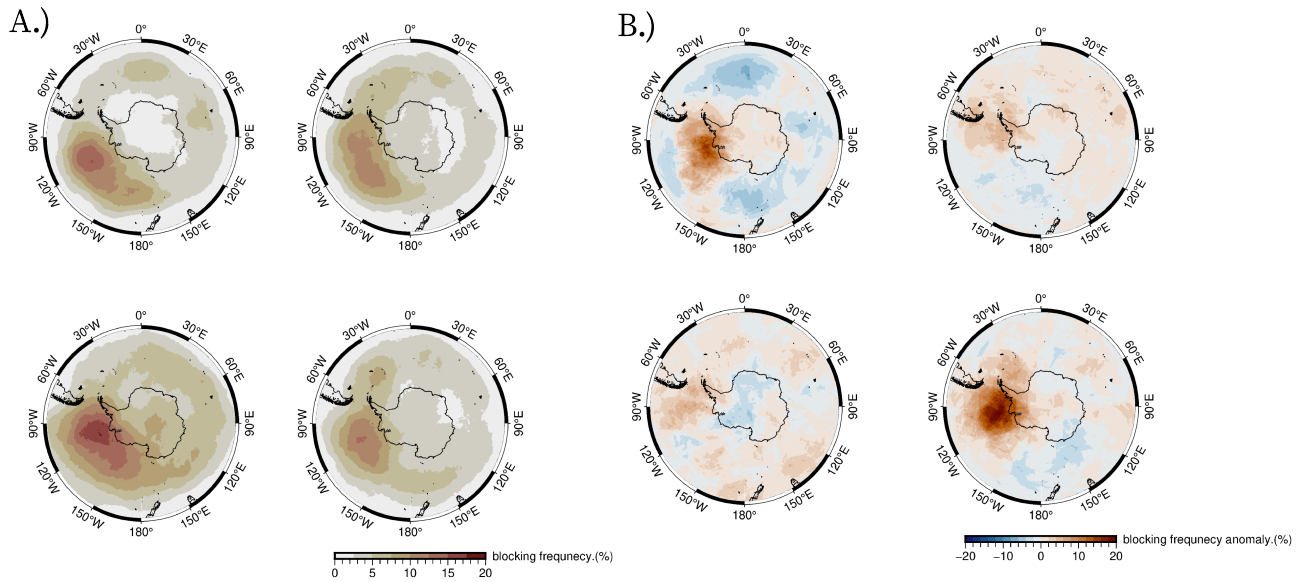
Figure 10. (A) Seasonal blocking frequency cycle and the (B) blocking frequency anomalies associated with extreme precipitation on Thwaites Glacier.

435 rivers account for 8% of the total accumulation measured at the sites of the long-term GNSS receivers over the ~~10~~ ten years of available observations. In total, we identify ~~19~~ 12 atmospheric river events~~that~~, defined as continuous periods (multiple hours to multiple days), when rivers make landfall within ~~5~~ 5 days of an extreme accumulation event observed with GNSS-IR (90th percentile). ~~Some of these events are not necessarily distinct (i.e. they occur within three days of other atmospheric rivers and could be considered part of the same vapor transport anomaly). The twelve~~ The 12 distinct events are shown in Figure 4 with

440 the accumulation that we observe at the inland GNSS-IR sites.

2.2.3 Summer and winter teleconnections

Composite anomalies of sea surface temperature and geopotential height at the 500 hPa pressure level were analyzed across the Southern Hemisphere to posit and test the significance of tropical teleconnections that may drive extreme winter and summertime precipitation in the Amundsen Sea. In the austral winter, we find significant positive tropical Atlantic, southeastern

445 Atlantic, and southwestern Indian Ocean sea surface temperature anomalies preceding extreme snowfall on Thwaites Glacier (Figure 11, Supplementary Figure S3). We also identify a clear train of alternating high and low-pressure anomalies consistent with Rossby waves that migrate eastward building up to extreme precipitation events (Figure 12, Supplementary Figures S3, S4, S5, S6, S7). In the austral winter, these Rossby wave trains, as expressed in 500 hPa pressure anomalies, extend from large anomalies off the coast of Africa in the eastern Atlantic 4-5 days preceding the extreme precipitation event (Figure 12). These

450 waves propagate across the Southern Ocean to the Amundsen and Bellingshausen Seas. In austral summer, the anomalies associated with extreme precipitation events are stronger and more significant in the Bellingshausen Sea and appear to be
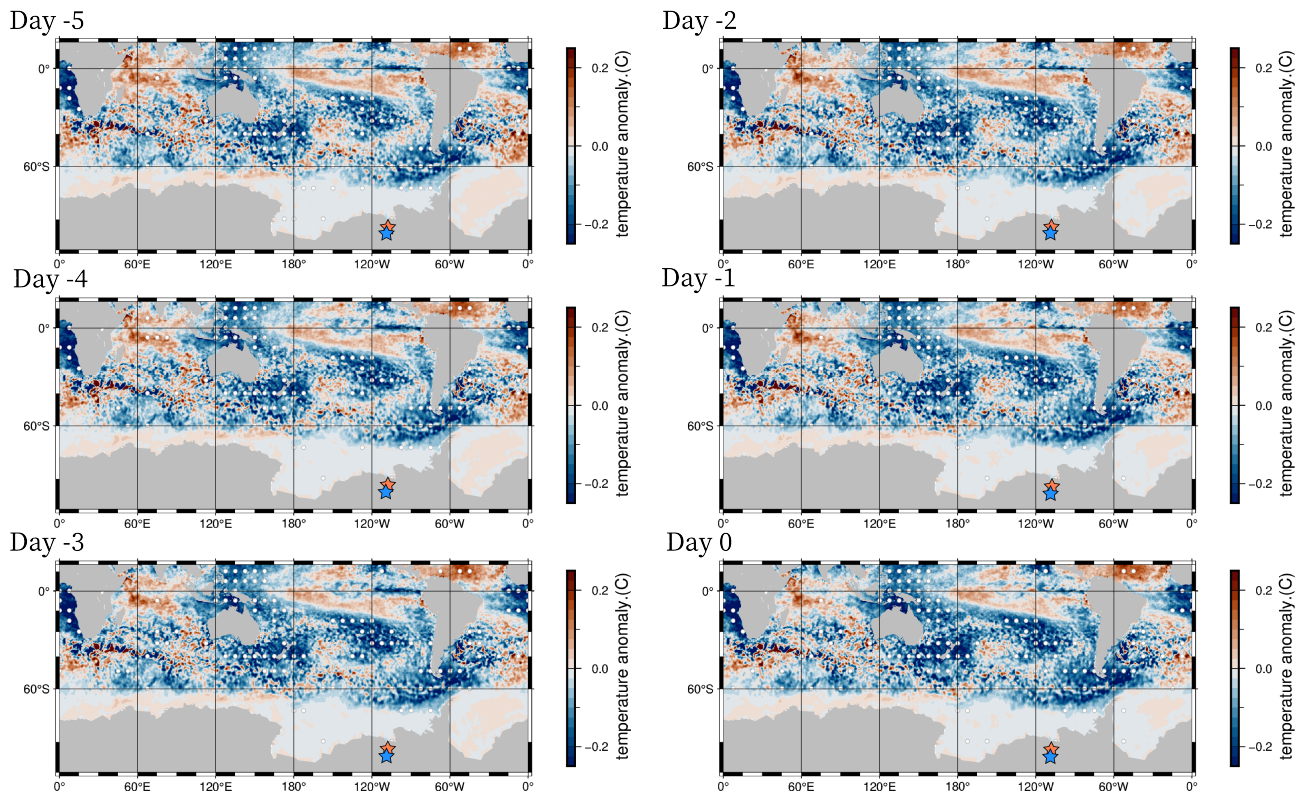
Figure 11. Austral winter sea surface temperature anomalies. Days for each panel indicate the shifted index for composite average prior to (or on) the day of extreme precipitation observed at the GNSS-IR stations located on Thwaites Glacier, which are plotted as orange and blue stars.

driven by significant summer sea surface temperature anomalies in the central Pacific, in addition to significant anomalies in the Atlantic and western Indian oceans (Supplementary Figures S2, S3).

3   Discussion

455   The character ~~and strength~~ of the Amundsen Sea Low, specifically the magnitude of the low-pressure anomaly and the location of the anomaly, ~~have~~ has historically been the climatological ~~indices~~ index most well-linked to accumulation variability in the Amundsen Sea Embayment~~and have~~, and has been used to suggest connections between synoptic atmospheric variability and West Antarctic precipitation. These indices represent a mean anomaly integrating pressure variations over many days and many different synoptic conditions, which complicates the interpretation and attribution of signals that might promote extreme

460   events. Chittella et al. (2022) showed that the second principal component of the geopotential height at 850 hPa~~(~~, which is correlated to the 500hPa geopotential height analyzed in our study~~)~~, is highly correlated ($r^2 = 0.9$) with the ~~longitudinal~~ zonal position of the Amundsen Sea Low and explains 43% of the extreme precipitation events observed over this period. Our data,
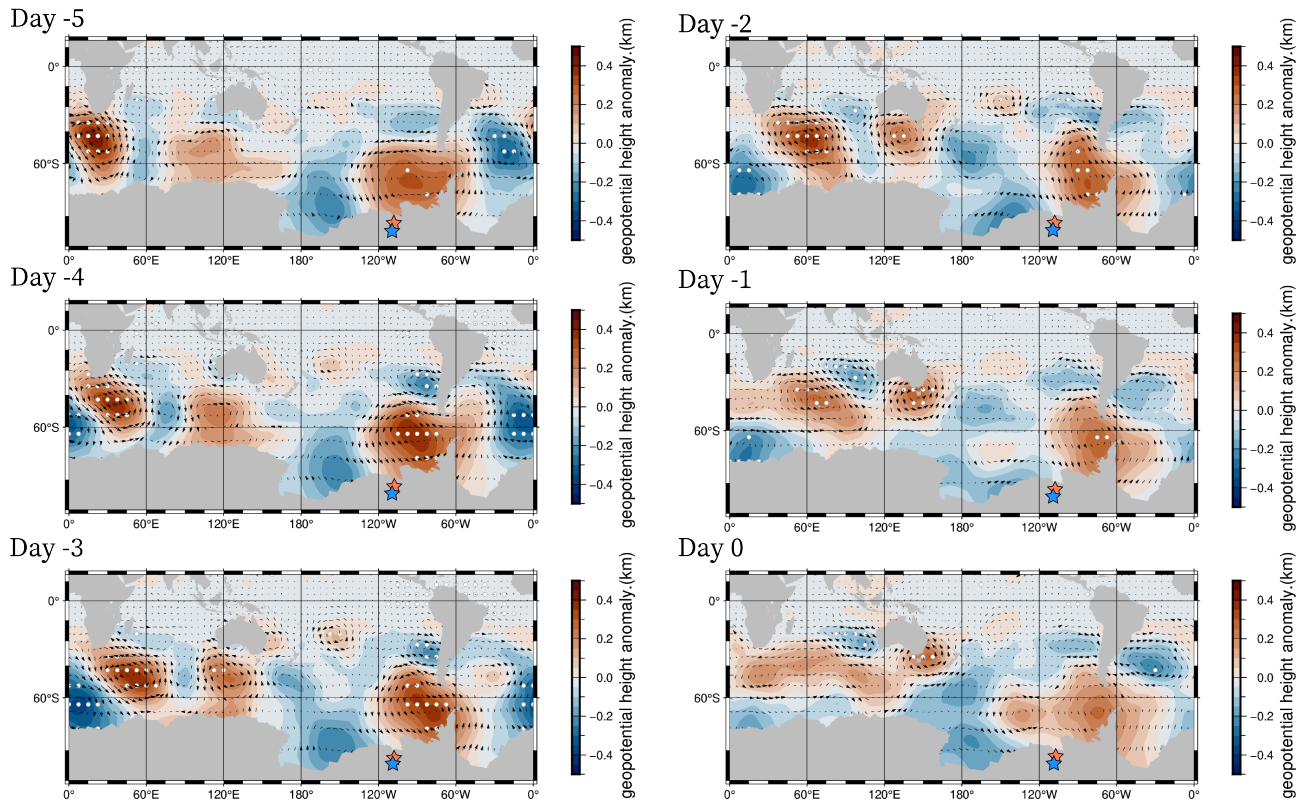
Figure 12. Austral winter geopotential height anomalies at the 500 hPa pressure level. Days for each panel indicate the shifted index for composite average prior to (or on) the day of extreme precipitation observed at the GNSS-IR stations located on Thwaites Glacier, which are plotted as orange and blue stars.

in conjunction with interpretations of regional reanalysis and other studies that use similar reanalysis products (Maclennan and Lenaerts, 2021; Chittella et al., 2022), suggest blocking highs in the ~~Bellinghausen~~ Bellingshausen Sea drive extreme vapor

465 transport into the ~~WAIS~~ West Antarctic interior (Figures 4, 8, 10). This pattern has previously been shown to be responsible for high snowfall events over Thwaites Glacier (Maclennan and Lenaerts, 2021; Chittella et al., 2022), and these ~~modeling~~ reanalysis studies agree with accumulation observations from GNSS interferometric reflectometry presented here~~. Though,~~ , though, in general, reanalysis underestimates extreme event frequency.

The GNSS-IR time series suggests that enhanced snowfall events observed in the ASE are associated with the blocking of

470 the westerly polar jet stream and resulting perturbations in the composite integrated water vapor transport. Patterns in vapor transport anomalies associated with extreme precipitation on Thwaites Glacier suggest that the polar storm track is blocked and that storms are re-routed poleward with distinct southward transport toward the Amundsen Sea. This is similar to the behavior observed over Greenland in the Northern Hemisphere, where mid-latitude high-pressure systems over Europe and the Eastern

Atlantic have been observed to divert storm tracks that then promote snowfall over Greenland (Pettersen et al., 2022).

Blocking in the Amundsen and Bellingshausen Seas exhibits a seasonal cycle that may explain the frequency of extreme precipitation, which controls over half of the total accumulation we observe with GNSS-IR in the Amundsen Sea Embayment. Indeed, 40% of extreme precipitation events were accompanied by blocking in the Amundsen and Bellingshausen sectors, and blocking frequency anomalies associated with extreme precipitation become more significant in summer and spring when blocking is generally less frequent than in winter. Increases in winter extreme precipitation event frequency compared to summer appear to be the result of Rossby wave breaking from convection northwest of the Amundsen and Bellingshausen Seas in the Atlantic, Indian, and western Pacific Ocean basins. These Rossby waves form a low-pressure anomaly to the west of Thwaites Glacier and a high-pressure anomaly to the east of Thwaites Glacier, funneling moisture from the tropics between the cyclone and anticyclone. In the austral summer, extratropical Rossby wave propagation still appears to play a role in routing moisture to the Amundsen Sea; however, the anomaly associated with the blocking high-pressure system in the Bellingshausen and Amundsen Seas extends further westward than the austral winter high-pressure system. This is consistent with Rossby wave propagation from the central Pacific and the significant positive sea-surface temperature anomalies observed there preceding extreme summer precipitation.

Previous numerical modeling experiments investigating tropical teleconnections to the Southern Hemisphere have suggested that Rossby wave propagation to the Amundsen Sea is driven primarily from the Indian and Atlantic basins northwest of the Amundsen Sea (Li et al., 2014; Simpkins et al., 2014; Li et al., 2015). Li et al. (2015) used idealized CAM4 simulations to show that anomalous convection events in the extratropical ocean basins in the Southern Hemisphere promote Rossby wave propagation that sums linearly in the southern Pacific Ocean. This complicates connecting the pressure anomalies and mechanisms that promote blocking in the Amundsen Sea to Rossby wave source mechanisms from specific basins. There are likely contributions from many different basins. This may explain the more complex pressure anomaly pattern observed in the summer when extreme precipitation is preceded by positive sea surface temperature anomalies in the central and western Pacific Ocean in addition to the Indian Ocean. During our study period, the pressure anomalies in winter, when it snows the most in the Amundsen Sea, resemble Rossby wave trajectories initiated from the subtropical Atlantic. Li et al. (2014) found the trajectory of the Rossby wave ray path to be similar in all seasons, first propagating poleward from the subtropical South Atlantic until waves were reflected by weak vorticity gradients in the polar region. In the austral summer, Li et al. (2015) found that rays continue propagating poleward until they dissipate at high latitudes; in austral winter, however, the rays interact with a second reflecting surface created by anticyclonic shear associated with the poleward flank of the subtropical jet and the equatorial flank of the mid-latitude jet stream. This reflecting surface is sufficiently strong in idealized model representations of Rossby wave propagation to steer the ray path of the waves to the Amundsen/Bellingshausen region. Significant sea surface temperature anomalies observed in the Atlantic and western Indian Ocean preceding extreme precipitation we composite using our GNSS-IR record are consistent with the propagation paths of eastward propagating Rossby waves modeled in the Southern Ocean (Li et al., 2015).

The advection of moist air masses by blocking anticyclones leads to precipitation in ~~the West Antarctic sector~~ West Antarctica and represents the dominant positive contribution to the Amundsen Sea Embayment surface mass balance. The ~~anomalous~~ anomalously warm 2 m air temperatures and water vapor transport along the coast of the continent also suggest that these pressure systems promote the transport of warm air and clouds that can insulate the continent when the snow is deposited. This has implications for the interpretation of ice cores in West Antarctica and the assimilation of ice-core data into paleoclimate reanalyses because the fractionation of isotopes is typically related to the local temperature of the precipitating cloud. The seasonality in accumulation we observe in the GNSS-IR time series and reanalysis suggests that austral winter conditions and associated inferences of atmospheric temperature are sampled more than austral summer conditions in firn and ice cores. Our results also suggest that archives from West Antarctica for all seasons are likely biased toward the conditions associated with extreme precipitation.

The blocking pressure field that has been identified here and in previous studies as promoting extreme precipitation has also been connected to melting in West Antarctica and may increase the likelihood of rainfall instead of snowfall at the surface as ~~the~~ this sector warms (Niwano et al., 2021). At present, the processes contributing water to the near-surface cannot sustain a perennial firn ~~aquifer~~ aquife, and melt refreezes due to the cold content of the firn. Meltwater refreezing raises the temperature of firn, which can promote additional surface melt in successive events. Meltwater production and refreezing also deplete the firn air content, which has preceded hydrofracture-induced ice-shelf breakup on the Antarctic Peninsula. Changes in the firn air content associated with melting and strain-induced thinning have poorly constrained impacts on the future integrity and susceptibility of the near-surface to hydrofracture and deserve further study.

Another important implication of this work is the key role of processes that are poorly captured in General Circulation Models, which do not reproduce the recent increasing trend in geopotential heights in the Amundsen and Bellingshausen Seas and tend to underestimate extreme event frequency and blocking frequency in the broader southern Pacific region. This contributes to inaccuracies in the simulation of West Antarctic snowfall ~~represented~~ in General Circulation Models. These models can also have biases associated with meridional integrated water vapor transport that underestimate snow accumulation in polar regions (Espinoza et al., 2018; Guan and Waliser, 2017). ~~Our~~ In agreement with Emanuelsson et al. (2018), our study suggests that in order to accurately model snowfall over West Antarctica and, in particular, the surface mass balance of Thwaites Glacier, atmospheric blocking, moisture transport, and precipitation processes must be properly simulated.

4   Conclusions

Spatially sparse in-situ meteorological observations of snowfall in Antarctica are an impediment to assessing ~~the~~ mechanisms responsible for extreme snowfall in the ASE and the quality of snow accumulation simulated in climate reanalysis products. GNSS-IR inverse methods ~~provide a unique method to~~ quantify surface mass balance and should be applied more broadly to GNSS networks in Greenland and Antarctica. These new techniques are advantageous compared to conventional automatic weather stations (AWS) in several ways: (1) they require less equipment and power than AWS, (2) the observations represent a larger surface ~~areas that is~~ area and are less likely to be biased by the station installation itself, ~~and~~ (3) these measurements can

be made on GNSS sites that are deployed for other reasons, such as ice dynamic and solid Earth studies~~and studies that have already been archived as part of historical geodetic surveys~~, and (4) there exist a wealth of historical GNSS data that could be re-processed to produce accumulation time series from GNSS-IR. In this study, we use GNSS-IR to derive accumulation records for the long-term on-ice GNSS sites located in the ASE along with ~~three~~ two austral summers of campaign GNSS data. The GNSS-IR accumulation records reveal that precipitation on Thwaites Glacier is most frequent and intense in the austral winter (30 to 50% higher) with a peak accumulation in August that tapers into the austral summer to a minimum in January. The seasonal cycle is driven primarily by changes in the frequency of extreme precipitation events, which make up over half of total precipitation in the Amundsen Sea.

We use the GNSS-IR snow accumulation time series to interrogate the synoptic atmospheric conditions that promote vapor transport to the Amundsen Sea that precedes extreme precipitation events. We find that blocking plays an important role in driving extreme precipitation. The connection between seasonal blocking in the southeastern Pacific and precipitation events in West Antarctica has important implications for the mass balance of vulnerable outlet glaciers located in the Amundsen Sea Embayment. We find that accumulation in the Amundsen Sea varies seasonally and interannually and that much of this change can be explained by the presence of blocking high-pressure systems that promote extratropical cyclonic activity and vapor transport to the Amundsen Sea. This suggests that atmospheric blocking, moisture transport, and precipitation processes must be properly simulated in order to accurately model snowfall and surface mass balance over West Antarctica.

Code and data availability. Inverse methods are available at https://github.com/hoffmaao/thwaites-gnss-ir. GNSS reflection processing code is available at https://github.com/kristinemlarson/gnssrefl.

Video supplement. A video of the accumulation event observed in the 2007-2008 summer (SupplementMovie.gif) is available in the Supplementary Materials.

Appendix A: Atmospheric catalogs

A1 Blocking catalog

Atmospheric blocking is associated with stable shifts in the position of persistent high-pressure systems, which can impact the track of cyclonic storm systems. Blocking describes many different states of the atmosphere, and thus many different methods have been developed to identify and track blocking events from reanalysis data (Schwierz et al., 2004; Barriopedro et al., 2010). We use the absolute geopotential height reversal-based (AGP) blocking index to identify blocking highs and track their evolution between $40°$ and $90°$S, with a spatial overlap of a least five days based on the reversal of the geopotential height gradient at 500 hPa. The index was first implemented by Steinfeld and Pfahl (2019) and is a two-dimensional extension of the classical blocking index developed by Tibaldi and Molteni (1990), which follows from the description of (Rex, 1950).

A2 Atmospheric river catalog

We also catalog the atmospheric rivers that made landfall in the ASE between 1979 and 2021. Atmospheric rivers were identified using vertical integrals of specific humidity and horizontal wind from ERA5 reanalysis to calculate total integrated vapor transport (IVT):

$$IVT = \frac{1}{g} \int\limits_{surface}^{trop} qvdp + \frac{1}{g} \int\limits_{surface}^{trop} qudp \tag{A1}$$

where q is specific humidity, u is the zonal horizontal wind component, v is the meridional horizontal wind component, p is pressure, and g is the terrestrial gravitational constant. An event catalog was created using a threshold value defined monthly for each grid cell. This detection scheme first identified the 98th percentile of total IVT over a 5-month period centered on the month to be cataloged for each cell. The landfall location was then identified based on the intersection of the IVT anomaly with the Antarctic coastline. The axis of the IVT anomaly was calculated following Brands et al. (2017) and then was used to determine the length and aspect ratio of the anomaly along with the mean IVT direction and the mean IVT magnitude. Events were then filtered based on their geometry and the magnitude of the meridional component of IVT relative to a poleward threshold value. ~~Anomalies with a~~ IVT Anomalies are considered atmospheric rivers when the meridional to zonal aspect ratio of the IVT anomaly is greater than 2:1 and ~~a~~ the meridional component of ~~IVT~~ the IVT anomaly is larger than $100 kg \cdot m^{-1} s^{-1}$. The detection algorithm was applied to hourly fields of vertically integrated vapor transport from 1000 hPa to 300 hPa pressure levels to create an atmospheric river time series from 2008 to 2022 when continuous GNSS data on Thwaites Glacier were also available. Detected atmospheric river events presented here agree well with other catalogs made using similar methods (Wille et al., 2021).

Author contributions. AOH, MM, and JL theorized the study. AOH wrote the GNSS-IR accumulation inverse package, the atmospheric river event detection algorithm and implemented the blocking algorithm, MM derived accumulation histories from reanalysis for each of the GNSS sites, KL wrote the GNSS-IR processing package. All authors contributed to the drafting and editing of the manuscript.

Competing interests. The authors declare no conflicts of interest.

Acknowledgements. We thank Terry Wilson, and the UNVACO/POLENET teams for maintaining the GPS sites, particularly Joe Pettit, Marianne Okal, Thomas Nylon, and Nico Bayou. The work was supported by a NASA FINESST award (grant 80NSSC20K1627), the NASA sea-level change team (grant 80NSSC17K0698), and the NSF-NERC International Thwaites Glacier Collaboration (grant OPP-1738934). NOAA Interpolated Outgoing Longwave Radiation (OLR) data and NOAA Interpolated daily sea surface temperature (SST) data provided by the NOAA PSL, Boulder, Colorado, USA, from their website at https://psl.noaa.gov. We also recognize the efforts and thank the folks who maintain and post era5 reanalysis products.

References

Adusumilli, S., Fish, M., Fricker, H. A., and Medley, B.: Atmospheric River Precipitation Contributed to Rapid Increases in Surface Height of the West Antarctic Ice Sheet in 2019, Geophysical Research Letters, 48, https://doi.org/10.1029/2020gl091076, 2021.

Baines, P. G. and Fraedrich, K.: Topographic effects on the mean tropospheric flow patterns around Antarctica, Journal of Atmospheric Sciences, 46, 3401–3415, 1989.

Barletta, V. R., Bevis, M., Smith, B. E., Wilson, T., Brown, A., Bordoni, A., Willis, M., Khan, S. A., Rovira-Navarro, M., Dalziel, I., et al.: Observed rapid bedrock uplift in Amundsen Sea Embayment promotes ice-sheet stability, Science, 360, 1335–1339, 2018.

Barriopedro, D., García-Herrera, R., and Trigo, R. M.: Application of blocking diagnosis methods to General Circulation Models. Part I: a novel detection scheme, Climate Dynamics, 35, 1373–1391, https://doi.org/10.1007/s00382-010-0767-5, 2010.

Brands, S., Gutiérrez, J. M., and San-Martín, D.: Twentieth-century atmospheric river activity along the west coasts of Europe and North America: algorithm formulation, reanalysis uncertainty and links to atmospheric circulation patterns, Climate Dynamics, 48, 2771–2795, https://doi.org/10.1007/s00382-016-3095-6, 2017.

Chen, G.: GPS kinematic positioning for the airborne laser altimetry at Long Valley, California, Ph.D. thesis, Massachusetts Institute of Technology, 1998.

Chittella, S. P. S., Deb, P., and Wessem, J. M. v.: Relative Contribution of Atmospheric Drivers to "Extreme" Snowfall Over the Amundsen Sea Embayment, Geophysical Research Letters, 49, https://doi.org/10.1029/2022gl098661, 2022.

Christian, J. E., Robel, A. A., Proistosescu, C., Roe, G., Koutnik, M., and Christianson, K.: The contrasting response of outlet glaciers to interior and ocean forcing, The Cryosphere, 14, 2515–2535, https://doi.org/10.5194/tc-14-2515-2020, 2020.

Connolley, W. M.: Variability in annual mean circulation in southern high latitudes, Climate Dynamics, 13, 745–756, https://doi.org/10.1007/s003820050195, 1997.

Dalaiden, Q., Goosse, H., Lenaerts, J. T. M., Cavitte, M. G. P., and Henderson, N.: Future Antarctic snow accumulation trend is dominated by atmospheric synoptic-scale events, Communications Earth & Environment, 1, 62, https://doi.org/10.1038/s43247-020-00062-x, 2020.

Davison, B. J., Hogg, A. E., Rigby, R., Veldhuijsen, S., van Wessem, J. M., van den Broeke, M. R., Holland, P. R., Selley, H. L., and Dutrieux, P.: Sea level rise from West Antarctic mass loss significantly modified by large snowfall anomalies, Nature Communications, 14, 1479, https://doi.org/10.1038/s41467-023-36990-3, 2023.

Dawson, A.: Windspharm: A high-level library for global wind field computations using spherical harmonics, Journal of Open Research Software, 4, 2016.

Ding, Q., Steig, E. J., Battisti, D. S., and Wallace, J. M.: Influence of the tropics on the southern annular mode, Journal of Climate, 25, 6330–6348, 2012.

Emanuelsson, B. D., Bertler, N. A. N., Neff, P. D., Renwick, J. A., Markle, B. R., Baisden, W. T., and Keller, E. D.: The role of Amundsen–Bellingshausen Sea anticyclonic circulation in forcing marine air intrusions into West Antarctica, Climate Dynamics, 51, 3579–3596, https://doi.org/10.1007/s00382-018-4097-3, 2018.

Espinoza, V., Waliser, D. E., Guan, B., Lavers, D. A., and Ralph, F. M.: Global Analysis of Climate Change Projection Effects on Atmospheric Rivers, Geophysical Research Letters, 45, 4299–4308, https://doi.org/10.1029/2017gl076968, 2018.

Fogt, R. L., Wovrosh, A. J., Langen, R. A., and Simmonds, I.: The characteristic variability and connection to the underlying synoptic activity of the Amundsen-Bellingshausen Seas Low, Journal of Geophysical Research: Atmospheres, 117, n/a–n/a, https://doi.org/10.1029/2011jd017337, 2012.

Frezzotti, M., Scarchilli, C., Becagli, S., Proposito, M., and Urbini, S.: A synthesis of the Antarctic surface mass balance during the last 800 yr, The Cryosphere, 7, 303–319, https://doi.org/10.5194/tc-7-303-2013, 2013.

Frieler, K., Clark, P. U., He, F., Buizert, C., Reese, R., Ligtenberg, S. R. M., Broeke, M. R. v. d., Winkelmann, R., and Levermann, A.: Consistent evidence of increasing Antarctic accumulation with warming, Nature Climate Change, 5, 348–352, https://doi.org/10.1038/nclimate2574, 2015.

Fudge, T. J., Markle, B. R., Cuffey, K. M., Buizert, C., Taylor, K. C., Steig, E. J., Waddington, E. D., Conway, H., and Koutnik, M.: Variable relationship between accumulation and temperature in West Antarctica for the past 31,000 years, Geophysical Research Letters, 43, 3795–3803, https://doi.org/10.1002/2016gl068356, 2016.

Gelaro, R., McCarty, W., Suárez, M. J., Todling, R., Molod, A., Takacs, L., Randles, C. A., Darmenov, A., Bosilovich, M. G., Reichle, R., Wargan, K., Coy, L., Cullather, R., Draper, C., Akella, S., Buchard, V., Conaty, A., da Silva, A. M., Gu, W., Kim, G.-K., Koster, R., Lucchesi, R., Merkova, D., Nielsen, J. E., Partyka, G., Pawson, S., Putman, W., Rienecker, M., Schubert, S. D., Sienkiewicz, M., and Zhao, B.: The Modern-Era Retrospective Analysis for Research and Applications, Version 2 (MERRA-2), Journal of Climate, 30, 5419 – 5454, https://doi.org/https://doi.org/10.1175/JCLI-D-16-0758.1, 2017.

Guan, B. and Waliser, D. E.: Atmospheric rivers in 20 year weather and climate simulations: A multimodel, global evaluation, Journal of Geophysical Research: Atmospheres, 122, 5556–5581, https://doi.org/10.1002/2016jd026174, 2017.

Hansen, J. S., Dukin, W. J., Willis, M. J., Wilson, T. J., Bevis, M. G., and Gómez, D. D.: Sensitivity of Modeled Elastic Deformation in the Amundsen Sea Embayment, Authorea Preprints, 2023.

Hersbach, H., Bell, B., Berrisford, P., Hirahara, S., Horányi, A., Muñoz-Sabater, J., Nicolas, J., Peubey, C., Radu, R., Schepers, D., Simmons, A., Soci, C., Abdalla, S., Abellan, X., Balsamo, G., Bechtold, P., Biavati, G., Bidlot, J., Bonavita, M., Chiara, G., Dahlgren, P., Dee, D., Diamantakis, M., Dragani, R., Flemming, J., Forbes, R., Fuentes, M., Geer, A., Haimberger, L., Healy, S., Hogan, R. J., Hólm, E., Janisková, M., Keeley, S., Laloyaux, P., Lopez, P., Lupu, C., Radnoti, G., Rosnay, P., Rozum, I., Vamborg, F., Villaume, S., and Thépaut, J.: The ERA5 global reanalysis, Quarterly Journal of the Royal Meteorological Society, 146, 1999–2049, https://doi.org/10.1002/qj.3803, 2020.

Hoffman, A. O., Christianson, K., Shapero, D., Smith, B. E., and Joughin, I.: Brief Communication: Heterogenous thinning and subglacial lake activity on Thwaites Glacier, West Antarctica, The Cryosphere, 14, 4603–4609, https://doi.org/10.5194/tc-2020-80, 2020.

Holton, J. R.: An introduction to dynamic meteorology, American Journal of Physics, 41, 2004.

Hosking, J. S., Orr, A., Marshall, G. J., Turner, J., and Phillips, T.: The Influence of the Amundsen–Bellingshausen Seas Low on the Climate of West Antarctica and Its Representation in Coupled Climate Model Simulations, Journal of Climate, 26, 130315144221 005, https://doi.org/10.1175/jcli-d-12-00813.1, 2013.

Jones, T. R., Cuffey, K. M., Roberts, W. H. G., Markle, B. R., Steig, E. J., Stevens, C. M., Valdes, P. J., Fudge, T. J., Sigl, M., Hughes, A. G., Morris, V., Vaughn, B. H., Garland, J., Vinther, B. M., Rozmiarek, K. S., Brashear, C. A., and White, J. W. C.: Seasonal temperatures in West Antarctica during the Holocene, Nature, 613, 292–297, https://doi.org/10.1038/s41586-022-05411-8, 2023.

Joughin, I., Tulaczyk, S., Bamber, J. L., Blankenship, D., Holt, J. W., Scambos, T., and Vaughan, D. G.: Basal conditions for Pine Island and Thwaites Glaciers, West Antarctica, determined using satellite and airborne data, Journal of Glaciology, 55, 245–257, https://doi.org/10.3189/002214309788608705, 2009.

Kaspari, S., Mayewski, P. A., Dixon, D. A., Spikes, V. B., Sneed, S. B., Handley, M. J., and Hamilton, G. S.: Climate variability in West Antarctica derived from annual accumulation-rate records from ITASE firn/ice cores, Annals of Glaciology, 39, 585–594, https://doi.org/10.3189/172756404781814447, 2004.

King, M.: Rigorous GPS data-processing strategies for glaciological applications, Journal of Glaciology, 50, 601–607, https://doi.org/10.3189/172756504781829747, 2004.

Lachlan-Cope, T. and Connolley, W.: Teleconnections between the tropical Pacific and the Amundsen-Bellinghausens Sea: Role of the El Niño/Southern Oscillation, Journal of Geophysical Research: Atmospheres, 111, 2006.

Lachlan-Cope, T. A., Connolley, W. M., and Turner, J.: The role of the non-axisymmetric antarctic orography in forcing the observed pattern of variability of the Antarctic climate, Geophysical Research Letters, 28, 4111–4114, https://doi.org/10.1029/2001gl013465, 2001.

Larson, K. M., Gutmann, E. D., Zavorotny, V. U., Braun, J. J., Williams, M. W., and Nievinski, F. G.: Can we measure snow depth with GPS receivers?, Geophysical Research Letters, 36, https://doi.org/10.1029/2009gl039430, 2009.

Larson, K. M., Wahr, J., and Munneke, P. K.: Constraints on snow accumulation and firn density in Greenland using GPS receivers, Journal of Glaciology, 61, 101–114, https://doi.org/10.3189/2015jog14j130, 2015.

Larson, K. M., MacFerrin, M., and Nylen, T.: Brief Communication: Update on the GPS reflection technique for measuring snow accumulation in Greenland, The Cryosphere, 14, 1985–1988, https://doi.org/10.5194/tc-14-1985-2020, 2020.

Lazzara, M. A., Weidner, G. A., Keller, L. M., Thom, J. E., and Cassano, J. J.: Antarctic Automatic Weather Station Program: 30 Years of Polar Observation, Bulletin of the American Meteorological Society, 93, 1519 – 1537, https://doi.org/10.1175/BAMS-D-11-00015.1, 2012.

Lenaerts, J. T. M. and van den Broeke, M. R.: Modeling drifting snow in Antarctica with a regional climate model: 2. Results, Journal of Geophysical Research: Atmospheres, 117, https://doi.org/https://doi.org/10.1029/2010JD015419, 2012.

Li, X., Holland, D. M., Gerber, E. P., and Yoo, C.: Impacts of the north and tropical Atlantic Ocean on the Antarctic Peninsula and sea ice, Nature, 505, 538–542, https://doi.org/10.1038/nature12945, 2014.

Li, X., Gerber, E. P., Holland, D. M., and Yoo, C.: A Rossby Wave Bridge from the Tropical Atlantic to West Antarctica, Journal of Climate, 28, 2256–2273, https://doi.org/10.1175/jcli-d-14-00450.1, 2015.

Li, X., Cai, W., Meehl, G. A., Chen, D., Yuan, X., Raphael, M., Holland, D. M., Ding, Q., Fogt, R. L., Markle, B. R., Wang, G., Bromwich, D. H., Turner, J., Xie, S.-P., Steig, E. J., Gille, S. T., Xiao, C., Wu, B., Lazzara, M. A., Chen, X., Stammerjohn, S., Holland, P. R., Holland, M. M., Cheng, X., Price, S. F., Wang, Z., Bitz, C. M., Shi, J., Gerber, E. P., Liang, X., Goosse, H., Yoo, C., Ding, M., Geng, L., Xin, M., Li, C., Dou, T., Liu, C., Sun, W., Wang, X., and Song, C.: Tropical teleconnection impacts on Antarctic climate changes, Nature Reviews Earth & Environment, 2, 680–698, https://doi.org/10.1038/s43017-021-00204-5, 2021.

Liebmann, B. and Smith, C. A.: Description of a complete (interpolated) outgoing longwave radiation dataset, Bulletin of the American Meteorological Society, 77, 1275–1277, 1996.

Maclennan, M. L. and Lenaerts, J. T. M.: Large-Scale Atmospheric Drivers of Snowfall Over Thwaites Glacier, Antarctica, Geophysical Research Letters, 48, https://doi.org/10.1029/2021gl093644, 2021.

Maclennan, M. L., Lenaerts, J. T. M., Shields, C., and Wille, J. D.: Contribution of Atmospheric Rivers to Antarctic Precipitation, Geophysical Research Letters, 49, e2022GL100 585, https://doi.org/10.1029/2022gl100585, 2022a.

Maclennan, M. L., Lenaerts, J. T. M., Shields, C. A., Hoffman, A. O., Wever, N., Thompson-Munson, M., Winters, A. C., Pettit, E. C., Scambos, T. A., and Wille, J. D.: Climatology and surface impacts of atmospheric rivers on West Antarctica, The Cryosphere, 17, 865–881, https://doi.org/10.5194/tc-17-865-2023, 2022b.

Medley, B. and Thomas, E. R.: Increased snowfall over the Antarctic Ice Sheet mitigated twentieth-century sea-level rise, Nature Climate Change, 9, 34–39, https://doi.org/10.1038/s41558-018-0356-x, 2019.

Medley, B., Joughin, I., Das, S. B., Steig, E. J., Conway, H., Gogineni, S., Criscitiello, A. S., McConnell, J. R., Smith, B. E., Broeke, M. R., Lenaerts, J. T. M., Bromwich, D. H., and Nicolas, J. P.: Airborne-radar and ice-core observations of annual snow accumulation over Thwaites Glacier, West Antarctica confirm the spatiotemporal variability of global and regional atmospheric models, Geophysical Research Letters, 40, 3649–3654, https://doi.org/10.1002/grl.50706, 2013.

Medley, B., Joughin, I., Smith, B. E., Das, S. B., Steig, E. J., Conway, H., Gogineni, S., Lewis, C., Criscitiello, A. S., McConnell, J. R., Broeke, M. R. v. d., Lenaerts, J. T. M., Bromwich, D. H., Nicolas, J. P., and Leuschen, C.: Constraining the recent mass balance of Pine Island and Thwaites glaciers, West Antarctica, with airborne observations of snow accumulation, The Cryosphere, 8, 1375–1392, https://doi.org/10.5194/tc-8-1375-2014, 2014.

Niwano, M., Box, J. E., Wehrlé, A., Vandecrux, B., Colgan, W. T., and Cappelen, J.: Rainfall on the Greenland Ice Sheet: Present-Day Climatology From a High-Resolution Non-Hydrostatic Polar Regional Climate Model, Geophysical Research Letters, 48, https://doi.org/10.1029/2021gl092942, 2021.

Pettersen, C., Henderson, S. A., Mattingly, K. S., Bennartz, R., and Breeden, M. L.: The Critical Role of Euro-Atlantic Blocking in Promoting Snowfall in Central Greenland, Journal of Geophysical Research: Atmospheres, 127, https://doi.org/10.1029/2021jd035776, 2022.

Pinat, E., Defraigne, P., Bergeot, N., Chevalier, J.-M., and Bertrand, B.: Long-Term Snow Height Variations in Antarctica from GNSS Interferometric Reflectometry, Remote Sensing, 13, https://doi.org/10.3390/rs13061164, 2021.

Raphael, M. N.: A zonal wave 3 index for the Southern Hemisphere, Geophysical Research Letters, 31, https://doi.org/https://doi.org/10.1029/2004GL020365, 2004.

Raphael, M. N., Marshall, G. J., Turner, J., Fogt, R. L., Schneider, D., Dixon, D. A., Hosking, J. S., Jones, J. M., and Hobbs, W. R.: The Amundsen Sea Low: Variability, Change, and Impact on Antarctic Climate, Bulletin of the American Meteorological Society, 97, 111–121, https://doi.org/10.1175/bams-d-14-00018.1, 2016.

Renwick, J. A.: ENSO-related variability in the frequency of South Pacific blocking, Monthly Weather Review, 126, 3117–3123, 1998.

Renwick, J. A.: Southern Hemisphere circulation and relations with sea ice and sea surface temperature, Journal of Climate, 15, 3058–3068, 2002.

Renwick, J. A.: Persistent positive anomalies in the Southern Hemisphere circulation, Monthly Weather Review, 133, 977–988, 2005.

Rex, D. F.: Blocking Action in the Middle Troposphere and its Effect upon Regional Climate, Tellus, 2, 275–301, https://doi.org/10.1111/j.2153-3490.1950.tb00339.x, 1950.

Robel, A. A., Roe, G. H., and Haseloff, M.: Response of Marine-Terminating Glaciers to Forcing: Time Scales, Sensitivities, Instabilities, and Stochastic Dynamics, Journal of Geophysical Research: Earth Surface, 123, 2205–2227, https://doi.org/10.1029/2018jf004709, 2018.

Roesler, C. and Larson, K. M.: Software tools for GNSS interferometric reflectometry (GNSS-IR), GPS Solutions, 22, 80, https://doi.org/10.1007/s10291-018-0744-8, 2018.

Schoof, C.: Marine ice sheet stability, Journal of Fluid Mechanics, 698, 62–72, https://doi.org/10.1017/jfm.2012.43, 2012.

Schwierz, C., Croci-Maspoli, M., and Davies, H. C.: Perspicacious indicators of atmospheric blocking, Geophysical Research Letters, 31, n/a–n/a, https://doi.org/10.1029/2003gl019341, 2004.

Sergienko, O. and Haseloff, M.: Basal controls of the grounding line dynamics of buttresses marine ice sheets, Tech. rep., Copernicus Meetings, 2023.

Shean, D. E., Christianson, K., Larson, K. M., Ligtenberg, S. R. M., Joughin, I. R., Smith, B. E., Stevens, C. M., Bushuk, M., and Holland, D. M.: GPS-derived estimates of surface mass balance and ocean-induced basal melt for Pine Island Glacier ice shelf, Antarctica, The Cryosphere, 11, 2655–2674, https://doi.org/10.5194/tc-11-2655-2017, 2017.

Siegfried, M. R., Medley, B., Larson, K. M., Fricker, H. A., and Tulaczyk, S.: Snow accumulation variability on a West Antarctic ice stream observed with GPS reflectometry, 2007–2017, Geophysical Research Letters, 44, 7808–7816, https://doi.org/10.1002/2017gl074039, 2017.

750 Simpkins, G. R., McGregor, S., Taschetto, A. S., Ciasto, L. M., and England, M. H.: Tropical Connections to Climatic Change in the Extratropical Southern Hemisphere: The Role of Atlantic SST Trends, Journal of Climate, 27, 4923–4936, https://doi.org/10.1175/jcli-d-13-00615.1, 2014.

Sinclair, M. R.: A climatology of anticyclones and blocking for the Southern Hemisphere, Monthly Weather Review, 124, 245–264, 1996.

Smith, B., Fricker, H. A., Gardner, A. S., Medley, B., Nilsson, J., Paolo, F. S., Holschuh, N., Adusumilli, S., Brunt, K., Csatho, B., Harbeck,
755 K., Markus, T., Neumann, T., Siegfried, M. R., and Zwally, H. J.: Pervasive ice sheet mass loss reflects competing ocean and atmosphere processes, Science, 368, 1239–1242, https://doi.org/10.1126/science.aaz5845, 2020.

Spikes, V. B., Hamilton, G. S., Arcone, S. A., Kaspari, S., and Mayewski, P. A.: Variability in accumulation rates from GPR profiling on the West Antarctic plateau, Annals of Glaciology, 39, 238–244, https://doi.org/10.3189/172756404781814393, 2004.

Steig, E. J., Mayewski, P. A., Dixon, D. A., Kaspari, S. D., Frey, M. M., Schneider, D. P., Arcone, S. A., Hamilton, G. S., Blue Spikes,
760 V., Albert, M., and et al.: High-resolution ice cores from US ITASE (West Antarctica): development and validation of chronologies and determination of precision and accuracy, Annals of Glaciology, 41, 77–84, https://doi.org/10.3189/172756405781813311, 2005.

Steinfeld, D. and Pfahl, S.: The role of latent heating in atmospheric blocking dynamics: a global climatology, Climate Dynamics, 53, 6159–6180, https://doi.org/10.1007/s00382-019-04919-6, 2019.

Thomas, E. R., Hosking, J. S., Tuckwell, R. R., Warren, R. A., and Ludlow, E. C.: Twentieth century increase in snowfall in coastal West
765 Antarctica, Geophysical Research Letters, 42, 9387–9393, https://doi.org/10.1002/2015gl065750, 2015.

Tibaldi, S. and Molteni, F.: On the operational predictability of blocking, Tellus A, 42, 343–365, https://doi.org/10.1034/j.1600-0870.1990.t01-2-00003.x, 1990.

Trenberth, K. E., Branstator, G. W., Karoly, D., Kumar, A., Lau, N.-C., and Ropelewski, C.: Progress during TOGA in understanding and modeling global teleconnections associated with tropical sea surface temperatures, Journal of Geophysical Research: Oceans, 103,
770 14 291–14 324, https://doi.org/https://doi.org/10.1029/97JC01444, 1998.

Turner, J., Phillips, T., Hosking, J. S., Marshall, G. J., and Orr, A.: The Amundsen Sea low, International Journal of Climatology, 33, 1818–1829, https://doi.org/10.1002/joc.3558, 2013.

Turner, J., Phillips, T., Thamban, M., Rahaman, W., Marshall, G. J., Wille, J. D., Favier, V., Winton, V. H. L., Thomas, E., Wang, Z., van den Broeke, M., Hosking, J. S., and Lachlan-Cope, T.: The Dominant Role of Extreme Precipitation Events in Antarctic Snowfall Variability,
775 Geophysical Research Letters, 46, 3502–3511, https://doi.org/https://doi.org/10.1029/2018GL081517, 2019.

van Wessem, J. M., van de Berg, W. J., Noël, B. P. Y., van Meijgaard, E., Amory, C., Birnbaum, G., Jakobs, C. L., Krüger, K., Lenaerts, J. T. M., Lhermitte, S., Ligtenberg, S. R. M., Medley, B., Reijmer, C. H., van Tricht, K., Trusel, L. D., van Ulft, L. H., Wouters, B., Wuite, J., and van den Broeke, M. R.: Modelling the climate and surface mass balance of polar ice sheets using RACMO2 – Part 2: Antarctica (1979–2016), The Cryosphere, 12, 1479–1498, https://doi.org/10.5194/tc-12-1479-2018, 2018.

780 Velicogna, I., Mohajerani, Y., A, G., Landerer, F., Mouginot, J., Noel, B., Rignot, E., Sutterley, T., van den Broeke, M., van Wessem, M., and Wiese, D.: Continuity of Ice Sheet Mass Loss in Greenland and Antarctica From the GRACE and GRACE Follow-On Missions, Geophysical Research Letters, 47, e2020GL087 291, https://doi.org/https://doi.org/10.1029/2020GL087291, e2020GL087291 10.1029/2020GL087291, 2020.

Walsh, K. J., Simmonds, I., and Collier, M.: Sigma-coordinate calculation of topographically forced baroclinicity around Antarctica, Dynamics of Atmospheres and Oceans, 33, 1–29, 2000.

Weertman, J.: Stability of the Junction of an Ice Sheet and an Ice Shelf, Journal of Glaciology, 13, 3–11, https://doi.org/10.3189/s0022143000023327, 1974.

Wille, J. D., Favier, V., Gorodetskaya, I. V., Agosta, C., Kittel, C., Beeman, J. C., Jourdain, N. C., Lenaerts, J. T. M., and Codron, F.: Antarctic Atmospheric River Climatology and Precipitation Impacts, Journal of Geophysical Research: Atmospheres, 126, https://doi.org/10.1029/2020jd033788, 2021.